Anatomy of a fumarole field; drone remote sensing and petrological approaches reveal the degassing and alteration structure at La Fossa cone, Vulcano Island, Italy

Daniel Müller[1], Thomas R. Walter[1], Valentin R. Troll[2,3], Jessica Stammeier[1], Andreas Karlsson[4], Erica de Paolo[5], Antonino Fabio Pisciotta[6], Martin Zimmer[1], Benjamin De Jarnatt[1]

[1] GFZ German Research Centre for Geosciences, Telegrafenberg, 14473 Potsdam, Germany
[2] Dept. of Earth Sciences, Natural Resources and Sustainable Development, Uppsala University, Sweden
[3] Istituto Nazionale di Geofisica e Vulcanologia (INGV), Rome, Italy
[4] Department of Geosciences, Swedish Museum of Natural History, Box 50007, SE-104 05 Stockholm, Sweden
[5] University of Milano-Bicocca, Department of Earth and Environmental Sciences, Piazza della Sciencza 4 – 20126 Milano, Italy
[6] Istituto Nazionale di Geofisica e Vulcanologia (INGV), Palermo, Italy

Correspondence to: Daniel Müller (dmueller@gfz-potsdam.de)

Abstract. Hydrothermal alteration and mineralization processes can affect the physical and chemical properties of volcanic rocks. Aggressive acidic degassing and fluid flow systems often lead to changes in the appearance of a rock, such as changes in surface coloration or intense bleaching. Hydrothermal alteration can have far-reaching consequences for rock stability and permeability, yet limited knowledge exists on the detailed structures, extent, and dynamic changes that take place near the surface of hydrothermal venting systems. By integrating drone-based photogrammetry with mineralogical and chemical analyses of rock samples and surface gas flux, we investigate the structure of the evolving volcanic degassing and alteration system at the La Fossa cone on the island of Vulcano, Italy. Our image analysis combines Principal Component Analysis (PCA) with image classification and thermal analysis, through which we identify an area of approximately 70,000 m² that outlines the maximum extent of hydrothermal alteration effects at the surface, represented by a shift in rock color from reddish to gray. Within this area, we identify distinct gradients of surface coloration and temperature that indicate a local variability of degassing and alteration intensity and define several structural units within the fumarole field. At least seven of such larger units of increased activity could be constrained. Through mineralogical and geochemical analysis of samples from the different alteration units, we define a relationship between surface appearance in drone imagery and the mineralogical and chemical composition. Alteration gradients in surface color from reddish to gray correlate with a reduction of Fe_2O_3 from up to 3.2 % in the unaltered regime to 0.3 % in the altered regime, and the latter coincides with the area of increased diffuse acid gas flux. As the pixel brightness increases towards higher alteration gradients, we note a loss of the initial (igneous) mineral fraction and a change in bulk chemical composition with a concomitant increase in sulfur content from close to 0 % in the unaltered samples to up to 60 % in samples from the altered domains. Using this approach of combined remote sensing and in situ analyses, we define and spatially constrain several alteration units and compare them to the present-day thermally active surface and degassing pattern over the main crater area. The combined results permit us to present a detailed anatomy of the La Fossa fumarole field, including high-temperature fumaroles and seven larger units of increased alteration intensity, surface temperature, and variably intense surface degassing. Importantly, we also identify apparently sealed surface domains that prevent degassing, likely as a consequence of mineral precipitation from degassing and alteration processes. By assessing the thermal energy release of the identified spatial units quantitatively, we show that thermal radiation of high-temperature fumaroles accounts for < 50 % of the total thermal energy release only, and that the larger part is emitted by diffuse degassing units. The integrated use of methods presented here has proven to be a useful combination for a detailed characterisation of alteration and activity patterns of volcanic degassing sites and has potential for application in alteration research and for monitoring of volcanic degassing systems.

1 Introduction

1.1 Volcanic degassing and hydrothermal alteration

Volcanic degassing at the Earth's surface is typically expressed in the form of localized fumarole fields and diffuse degassing. Yet, the association of localized and diffuse degassing is not well constrained. A fumarole is a vent or opening in the Earth's surface that releases steam and gas, including sulfur dioxide, carbon dioxide, and hydrogen sulfide, into the atmosphere (e.g. Giggenbach, 1996; Giammanco et al., 1998; Halldorsson et al., 2013). Fumaroles are typically found near volcanic areas or geothermal regions where there is intense heat beneath the surface. Fumaroles are of interest to scientists studying volcanoes and geothermal systems, as they provide information on the composition of underlying magmatic systems, the degassing processes of such magmatic systems, and the dynamic changes in the degassing passways exploited by such systems (e.g. Chiodini et al., 1993; Aiuppa et al., 2005; Paonita et al., 2013). The gas emissions by fumaroles, moreover, provide information on the possible interaction between underground water and hot rocks or magma and thus the state of a hydrothermal system through time (e.g. Chiodini et al., 1993; Capasso et al., 2000; Nuccio et al., 2001; Troll et al., 2012; Paonita et al., 2013).

The degassing of hot and acid volcanic gasses leads to versatile fluid-rock interactions at the surrounding volcanic rock, summarized as hydrothermal alteration (Pirajno, 2009; Chiodini et al., 2013; Fulignati, 2020). Alteration can affect the mineral assemblage by dissolution and remineralization up to complete destruction of the original mineral matrix and eventually influence essential rock parameters with potentially far-reaching consequences for the shallow hydrothermal system and the stability of a volcanic building (Reid & Brien, 2001; Heap & Violay, 2021). Mechanical strength tests of hydrothermally altered rocks showed considerable mechanical weakening (e.g. Frolova et al., 2014; Heap et al., 2021a, Darmawan et al., 2022), which is usually accomplished by mineral dissolution and mineral re-precipitation that affect rock strength and permeability and can in cases even seal gas pathways. Hydrothermal alteration can thus lead to sealed rock masses and hence to pressure build-up in a shallow volcanic system and consequently influence volcanic activity (e.g. Heap et al., 2019) and increase the likelihood of flank deformation and collapse (Heap et al., 2021b). It is therefore important to better understand the degassing and alteration structures in active hydrothermal crater regions of hazardous volcanic systems.

In this study of the fumaroles of La Fossa Vulcano Island - Italy, we aim to detect and quantify alteration-related spatial and compositional parameters in order to provide improved insight into the dynamic changes of hydrothermal venting systems to help identify temporal and potentially critical developments and to better understand the associated features of diffuse and localized degassing.

1.2 Structure and extent of degassing sites

Recent advances in volcanic geothermal areas suggest that fumaroles are often only localized expressions of a much larger area of degassing (e.g. Toutain et al., 2009; Liuzzo et al., 2015). Indeed, fumaroles and hydrothermal degassing zones are often accompanied by broader fields of activity, characterized by diffuse degassing processes, associated mineral changes, and

93 intense surface recoloration (e.g. Donoghue et al., 2008; Berg et al., 2018; Darmawan et al., 2022) and fumaroles activity can
94 vary in time (Troll et al., 2012; Fischer et al., 2015) and in size (Lynch et al., 2013; Gertisser et al 2023). Previous works at
95 Vulcano, for instance, have shown that fumaroles are surrounded by extensive areas of diffuse degassing (Carapezza et al.,
96 2011; Chiodini et al., 2005; Manini et al., 2019). Our previous work showed that diffuse degassing leads to distinct zones of
97 activity that can be identified by temperatures and visual expression (Müller et al., 2021). Those diffuse zones are typically
98 constrained based on CO_2 measurements but are also subject to the diffuse flow of acid gas driving diffuse alteration processes.
99 However, these diffuse degassing and alteration processes are often difficult to recognize without specialized sampling
100 strategies (Toutain et al., 2009), leading to a limited understanding of the anatomy and extent of degassing and alteration
101 systems. Understanding the dynamic changes and internal architecture of hydrothermal activity of fumarole fields and the true
102 dimensions of their field of activity is of relevance for the study of volcanic activity and hazard potential.
103

104 **1.3 Surface effects and remote sensing of alteration**

105 Hydrothermal alteration can cause significant changes in the physical and chemical properties of volcanic rock, such as density,
106 compressive strength, and permeability (e.g. Donoghue et al., 2008, 2010; Berg et al., 2018; Heap et al., 2019; Darmawan et
107 al., 2022). The replacement of primary minerals by secondary minerals, element mobility of fluid-mobile components,
108 enrichment of refractory elements, and physical and textural changes of rock properties are often accompanied by changes in
109 the color or spectral reflectance characteristics and can be traced employing remote sensing techniques.
110 Several studies have investigated the relationship between coloration and hydrothermal alteration. The use of rock color or
111 spectral reflectance particularities as an indicator of alteration has been explored since the 1970s and led to the development
112 of a variety of remote sensing techniques using satellite imagery from ETRS multispectral imagery (Rowan et. al., 1976),
113 Landsat Thematic mapper mission (Carranza et al., 2002), ETM+ (Mia et al., 2012) or ASTER data (Di Tommaso et al., 2007)
114 or hyperspectral analysis (e.g. Van De Meer et al., 2012; Tayebi et al., 2015). These techniques can detect subtle changes in
115 color that may not be visible to the naked eye, allowing for the identification of mineral deposits (Mielke et al., 2016),
116 hydrothermal alteration, or volcano stability (Kereszturi et al., 2020).
117 However, for analyzing details of localized degassing and alteration systems, the resolution of satellite data often is a limiting
118 factor. Some of the best available optical satellite data have a resolution of 0.5 m in the nadir acquisition position. The
119 resolution of thermal satellite data is on the order of tens to hundreds of meters per pixel. That allows the general detection of
120 degassing and alteration systems, but the imaging of details of such systems requires the use of very high-resolution data.
121 Modern UAS (unmanned aerial systems) equipped with high-resolution sensors allow imaging of volcanic surfaces at cm
122 scales and, therefore, permit the analysis of degassing and alteration systems in great detail. In combination with Structure
123 from Motion (SfM) processing, they are efficient for first-site investigations and allow the creation of high-resolution structural
124 maps to identify structures of degassing systems to assist first-order hazard analysis or guide further in-depth studies.

1.4 Aim of the study

The aim of this work is to image and analyze the degassing and alteration structure of the La Fossa fumarole field and the wider field of activity and better understand the association of diffuse and localized degassing and alteration at degassing sites. We advance previous results (Müller et al., 2021) by considering new data, and by integrating them with the mineralogical and chemical analysis of alteration distribution in collected rock samples. We show systematic changes in the effects of alteration on the surface coloration and how drone-derived RGB data (Red, Green, Blue, standard color coding of images) can be used for the efficient detection and classification of degassing and alteration features. Combining UAS-based optical and infrared remote sensing with mineralogical- and geochemical analysis, and diffuse surface degassing measurements, we can infer the detailed anatomy of degassing and alteration systems at the surface, highlight active degassing domains versus areas of surface sealing, and determine their importance for the system based on their contribution to the total thermal energy release.

2 Study area

Vulcano is the southernmost of a group of 7 small volcanic islands forming the Aeolian Archipelago north of Sicily. They are located within the Aeolian Tindary Letojanni Fault System (ATLFS), an NNW-SSE striking local deformation belt connecting the central Aeolian Islands with the eastern section of Sicily (Barreca et al., 2014; Cultrera et al., 2017). The ATLFS is the interface between two larger tectonically active compartments, an extensive one in the northeast and a contractional one in the west (Cultrea et al., 2017). Frequent seismic activity and right lateral extensional displacements indicate ongoing tectonic activity (Billi et al., 2006) and the active shaping of the islands.

Vulcano is made up of volcanic edifices of which the northern section of the islands is the most recently active. The oldest volcanic activity at Vulcano is reported for 130 ka (De Astis et al., 2013). Six main stages of volcanic activity have been identified (De Astis et al.1997), of which the geologically younger active parts, the La Fossa Cone and Vulcanello, have been active during historical times <8 ka, showing mainly vulcanian and strombolian activity (De Astis et al., 2013). The last eruptive period of the La Fossa Cone from 1888-1890 was characterized by strong phreatic eruptions and witnessed and documented by Guiseppe Mercalli who later coined the term Vulcanian eruptions (Clarke et al., 2015).

Vulcano since then has been in a quiescent period and volcanic activity mainly expressed in degassing. Gases are provided from a magmatic-hydrothermal system fed by a shallow magmatic reservoir beneath La Fossa volcano. The hydrothermal system is likely to have been partitioned into a hypersaline brine and a vapor phase (Henley and McNabb, 1978). The denser brine phase is confined at depth and contributes to the formation of metasomatic facies observed in deep-seated xenoliths (Adrian et al., 2007). The vapor phase, enriched with SO_2, H_2S, HCl, and HF, ascends to the surface and partly emerges directly from the high-temperature fumarolic field (Bolognesi and D'Amore, 1993; Chiodini et al., 2000; Capasso et al., 1997).

Volcanic degassing is present throughout the entire central and northern part of the island concentrating in degassing clusters at Baja Di Levante, within Vulcano Porto, and in clusters along the base and summit of La Fossa Cone (Chiodini et al., 1996;

Carapezza et al., 2011; Diliberto et al., 2021; Inguaggiato et al., 2022 and many others) where frequently higher fluxes of CO_2 are observed. The most prominent degassing sites are the high-temperature fumaroles at the summit of Vulcano that occur in several clusters on the outer rims of La Fossa cone and are most prominent in the high-temperature fumarole field (Figure 1). Degassing at the summit of La Fossa is persistent but subject to fluctuations. Gases of the high-temperature fumaroles (HTF) emerge with temperatures > 300°C, but temperatures have been exceeded during previous volcanic crises (Harris et al., 2012; Diliberto, 2017). Temperatures of up to 690°C were reported in May 1993 by Chiodini et al. (1995).

Periods of unrest were accompanied by increasing fumarole temperatures (Harris et al., 2012; Diliberto, 2013; Madonia et al., 2013; Diliberto, 2017), increasing soil and groundwater temperatures (Capasso et al., 2014), changing gas compositions (Paonita et al., 2013), changes in gas flux (Inguaggiat et al., 2022), or a spatial growth of the fumarole field (Bukomirovic et al., 1997). The most recent crisis occurred in 2021 and led to increased thermal radiation (Coppola et al., 2022), deformation (INGV Bulletin reports), and localized structural changes like the formation of new major fumarole complexes. The rapid dynamics during volcanic crises and potentially negative effects of alteration on permeabilities, and therewith the potential to drain gases from the surface, highlight the importance of a better understanding of the structure and state of degassing systems. Early studies about the structural setup of the Grand Cratere fumarole field of the La Fossa Cone were provided by Bukumirovic et al. (1997) and later modified (Madonia et al., 2016; Harris et al., 2009). Fulignati et al. (1999) analyzed alteration facies at Vulcano and constrained the central crater region to be a large silicic alteration complex characterized by the presence of chalcedony and amorphous silica. Outwardly to the central silicic alteration zone, advanced argillic (alunite ± gypsum) alteration develops, probably originating from the progressive neutralization of the acid fluids by weathering and dilution by meteoric waters (Fulignati et al., 1998). Müller et al. (2021) previously showed that degassing and alteration can be traced from remote sensing data far beyond the extent of the high-temperature fumarole locations. Based on surface color variability due to degassing and alteration processes they showed evidence for a more complex setup with alteration gradients within the silicic alteration complex and important structural units that will be complemented here. Examples of degassing and alteration-related surface color variability are shown in Figure 2.

3 Data and methods

To analyze the degassing and alteration structure at Vulcano, we used a combination of UAS-derived remote sensing data (optical and thermal infrared imagery), image analysis, and field-based ground-truthing by mineralogical and geochemical analysis of rock samples and surface degassing measurements. A simplified sketch of the workflow is shown in Figure 3.

1) An anomaly detection (Chapter 3.2) based on UAS-derived data, employing image analysis techniques like Principal Component Analysis (PCA), and spectral and thermal classification (similar to Müller et al., 2021) provides the detailed optical and thermal anomaly pattern. Anomalies can be revealed based on slight color changes in the volcanic surface that occur due to degassing and hydrothermal alteration processes, or increased surface temperatures.

187 2) To verify observed anomalies, we carried out ground-truthing by mineralogical (XRD - X-Ray diffraction) and geochemical
188 (XRF - X-Ray fluorescence) lab analyses of representative rock samples. Further, we performed surface degassing
189 measurements to image the present-day degassing pattern and compared it to the observed anomaly pattern. Combining this
190 information we can infer a detailed anatomy of the degassing and alteration structure at the surface and define and parameterize
191 major structural units.
192 3) A temporal infrared monitoring carried out from 2018 to 2022, covering the volcanic crisis 2021 at Vulcano allows us to
193 monitor the thermal evolution and response of the identified units to an event of increased gas flow with further implications
194 of critical processes like localized surface sealing.
195 Details on the single analysis steps are provided below.

196
197 **3.1. Acquisition and processing of UAS-based optical and thermal infrared data**

198 The data acquisition was performed using a DJI Phantom 4 Pro quadcopter, equipped with a gimbal-stabilized 20 MP camera
199 with a real shutter system, recording up to 0.5 HZ. Optical overflights were performed in the daytime at an altitude of 150 m
200 above the fumarole field, ensuring a minimum overlap of 90 % for later photogrammetric processing. Thermal infrared image
201 data was acquired by a Flir Tau 2 radiometric thermal infrared camera system attached to the DJI Phantom 4 Pro. The FLIR
202 Tau 2 measures in the spectral range of thermal infrared between 7.5 and 13 µm, has a resolution of 640 x 512 pixels, and is a
203 fully radiometric sensor system. The infrared image data is recorded at 8 Hz by a Teax Thermal Capture 2 data logger. The
204 camera was attached to the copter with a standard camera bracket on a self-made carrier frame and is powered by an external
205 11.1 V lithium-polymer battery, supplying voltage to the camera system (transformed down to 5.2 V in) and to an external
206 GPS antenna (> 8 V required) which provides coordinates for each infrared image. Infrared overflights were performed in the
207 early morning hours, before the sun illuminates the crater area, to avoid disturbances of irregular surface heating due to solar
208 radiation exposure (Stevenson and Varley, 2008). In this way, we ensure to map the thermal signal from the hydrothermal
209 system exclusively.
210 All image data were processed using the Structure from Motion (SfM) approach in Agisoft Photoscan (Version 1.5.2.7838).
211 The image data were inspected and images were preselected ensuring an overlap of 90 %. Images of poor quality or out of
212 focus were excluded and only images of a constant flight altitude were used for the processing. This is particularly important
213 for the processing of infrared data, as varying altitudes might alter the radiation information due to changing pixel size to vent
214 ratios. The infrared data was pre-inspected in Thermoviewer 3.0 and exported in a 16-bit tiff format in grayscale. We followed
215 the typical workflow of sparse point cloud-, dense point cloud- and mesh generation, aiming to obtain a 3-dimensional model
216 and eventually orthomosaic, digital elevation model (DEM), and infrared mosaic. The original images and processing results
217 are roughly georeferenced, but their geolocation was optimized by manual co-registration using the ArcGIS georeferencing
218 toolbox. An overview of the acquired and processed data sets can be found in Table 1.

219

3.2 Anomaly detection - Principal Component Analysis (PCA) and spectral classification for alteration mapping

The alteration mapping was performed on an orthomosaic data set acquired in 2019 that due to poor fumarole activity provides an almost distortion-free image of the central crater region. The alteration structure was revealed, similar to Müller et al. (2021), by applying a Principal Component Analysis and image classification allowing further constraints on the zonation of the fumarole area and expanding the interpretation by geochemical and mineralogical analyses of rock samples for ground truthing. PCA is a statistical tool that was invented by Pearson (1901), further developed and widely applied in remote sensing or image analysis (e.g. Loughlin, 1991; Fauvel et al., 2009; Alexandris et al., 2017). It can detect and highlight optical anomalies within an RGB data set by transforming the data values of the initial RGB channels onto their perpendicular axes of the highest data variance (e.g. Abdi & Williams, 2010). This can be achieved in several ways. We used the PCA implemented in the ArcGIS image analysis toolbox (see ArcGIS online documentation for Principal Component Analysis), performing the following workflow. In the first step, an ellipse including all data points is calculated for each dimension (RGB). The main axes of these ellipses represent the Eigenvectors (direction of highest variance), and will be used as a new coordinate system for the data transformation. By transforming all data points onto this new coordinate system, we obtain Principal Components (PC) which are variance representations of the initial RGB image data and can be used to detect and highlight optical anomalies like color changes due to alteration processes (Müller et al., 2021, Darmawan et al., 2022). PCA further promotes a decorrelation of the initial RGB bands, a dimensionality reduction, and associated better data separability so that color variations, before expressed by changes in the three RGB bands (3-dimensional problem), can now be accessed in single bands, the single Principal Components (PC). While Principal Component 1 (PC) resembles ~91.3 % (95) of the initial data variance, it mainly shows brightness changes within the image. PC 2 and 3 contain 7.4 (4.5) and 2.3 (0.5) % of the data variance, resemble color changes, and are suitable to resolve optical anomalies related to hydrothermal alteration.

In our data, hydrothermally altered areas were defined based on the PC3, with pixel values > 85 representing hydrothermal alteration. We used this as a mask to crop the respective pixel locations from the original orthomosaic (RGB), resulting in a 16 Mio pixel alteration raster subset (RGB). This alteration raster subset allows for a more sensitive image analysis due to the reduced spectral range with respect to the original orthomosaic. Another iteration of PCA, now applied to the extracted alteration raster subset adjusts to the new reduced spectral range, as we are excluding all redundant data e.g. unaltered surface, and provide a variance representation of the altered surface exclusively. We classified the result in an unsupervised classification (implemented in ArcGIS, using a combination of Iso Cluster and Maximum Likelihood classification) with 32 classes. We decided on unsupervised classification as this is a more data-explorative way of exploring the pixel information, rather than classifying based on a spectral range constrained by training areas defined on pre-assumptions in a supervised classification. The 32 classes are chosen to obtain a high class resolution, as this is the highest number of classes possible in the unsupervised classification tool. By combining these classes in a way that they resemble larger optical spatial units, we eventually defined 3 Types of alteration surface (Types 1-3) and the unaltered surface (Type 4) and further analyzed their spectral characteristics and spatial distribution. Boxplots of the distribution of RGB values in the 32 classes and the spectral

253 range of Type 1-4 surfaces are shown in Appendix A. The optical structure of the fumarole field and alteration zone is similar

254 to the thermal structure and will be discussed in Chapter 4.2.

255

3.3 Infrared analysis - thermal structure and time series analysis

257 The SfM-derived infrared mosaic represents the thermal radiation in a 16-bit tiff format, resembling values between 0 and

258 65536. To obtain a temperature map from the IR mosaic we calculated the apparent pixel temperatures Tp by

259 $$Tp \text{ (in K)} = grayvalue * 0.04 \quad (1)$$

260

261 where Tp is the apparent pixel Temperature in K, the gray value is the radiation value of the original infrared mosaic and 0.04

262 is the scaling factor (radiometric resolution). The temperature map was used to define the thermal structure. We observed

263 several distinct thermal spatial units with temperatures significantly above the background temperature, that can be

264 distinguished in high-temperature fumaroles (HTF in the following) and areas of rather diffuse thermal surface heating (Figure

265 4 B/D). To constrain these units spatially for further comparison, we had to approximate spatial boundaries what was done

266 after comparison to our optical data and based on knowledge of previous observations by defining the temperature thresholds

267 of T = 22-40°C for the diffuse heated areas and T > 40°C for HTF. The 40°C threshold resembles well the known locations

268 and extent of HTF in the upper and lower fumarole field. To compare the thermal emissions of detected structural units, we

269 calculate the radiant exitance values by applying the modified Boltzmann law.

270 $$Q = e*b*A*(Tp^4 - To^4) \quad (2)$$

271 The emissivity (e) was assumed to be 0.95 (often used as an assumption for volcanic surfaces), the Boltzmann constant (b) is

272 5.670737×10^{-8} Wm-2K4, the area of a pixel (A) is 0.024 m². *Tp* is the pixel temperature and *To* is the average background

273 mean temperature, calculated based on 9 reference areas that are anomaly-free. To compare identified units quantitatively, we

274 summarized the radiation per pixel for the respective units a-g to a cumulative thermal radiation (Rcum). The flight altitude of

275 150 m (above the fumarole field) in combination with the low resolution of infrared sensors results in a pixel resolution of

276 0.38 x 0.38 m.

277 Note that remotely sensed Infrared data always represents apparent temperatures that might differ from the real object

278 temperature due to the radiation properties of the measured object itself (emissivity), the distance of the sensor to the measured

279 object, the pixel-to-object size ratio, but also due to atmospheric or hydro-meteorological effects (Ball and Pinkerton, 2006)

280 influencing the detected radiation values. Therefore apparent temperatures typically are lower than in situ vent temperatures.

281 Real fumarole vent temperatures can reach more than 300°C (Diliberto, 2013) while temperatures in our infrared mosaic range

282 to max. 163°C only. With this data set, we do not aim to provide precise fumarole temperatures but to analyze the thermal
283 structure of the fumarole field and the broader field of activity.

284

3.4 Ground-truthing by Mineralogical and Geochemical Analysis

3.4.1 Rock sampling

287 Rock samples were collected at predefined representative locations aiming to include all alteration end members, during field
288 campaigns in 2019 and 2022. We sampled along 3 transects following the postulated hydrothermal alteration gradients and
289 crosscutting major alteration units, of which transect A is located on the lower fumarole field, transect b along the upper crater
290 rim, and transect c is located in the eastern crater crosscutting several alteration units (locations for samples in Figure 7).
291 Samples were in the size of ~2000cm³ (hand-sized) retaining the undisturbed surface crust, but also subsurface material to a
292 depth of ~ 10 cm. The samples were mechanically crushed, ground to 63 µm, and split for XRD and XRF analysis, respectively.
293 In total 21 samples were collected of which 9 were prepared for the XRD and XRF analysis and 12 for XRF analysis
294 exclusively.

3.4.2 X-ray diffraction (XRD)

296 Between 1 and 3 mg of whole rock powder was used to determine the mineral composition of each sample through powder X-
297 ray diffraction (pXRD). The analysis was conducted using a PANalytical X'pert diffractometer equipped with an X'Celerator
298 silicon-strip detector at the Department of Geoscience, Swedish Museum of Natural History, Stockholm. The instrument was
299 operated at 45 kV and 40 mA using Cu-Kα radiation ($\lambda = 1.5406$ Å). Samples were analyzed between 5° and 70° (2θ) for 20
300 min in step sizes of 0.017° in continuous scanning mode while rotating the sample. Data were collected with "divergent slit
301 mode" and converted to "fixed slit mode" for Rietveld refinement. The collected data show several peaks of X-ray diffraction
302 intensity which represent the characteristic of crystalline minerals, the proportions of mineral phases were then refined using
303 the Rietveld refinement method in the High Score Plus 4.6e software. The XRD analytical procedure was performed twice for
304 each sample to ensure optimal quality control. Some samples contained contents of amorphous material of more than 50 %.
305 Those will be marked with a * in the following but we will consider the mineral composition normalized to 100 % non-
306 amorphous material.

3.4.3 X-ray fluorescence (XRF)

308 Bulk chemical composition was determined by X-ray fluorescence analysis (XRF) at the ElMiE Lab at the German Center for
309 Geosciences (GFZ). Main and trace elements were measured on fused beads with an AXIOS spectrometer (Malvern
310 Panalytical, UK). Loss of ignition (LOI) was determined by analysis of H_2O/CO_2 using an Eltra element analyzer.

311 Reproducibility was determined on three certified reference materials (CRM) and is within the analytical precision, which is
312 better than 2 % for main elements and better than 10 % for trace elements.

313 **3.4.4 Surface degassing measurements (CO_2, SO_2, H_2S)**

314 The surface degassing was measured at ~ 200 points within the northern part of the La Fossa cone (Figure 6) in September
315 2021 and November 2022 using a simplified multi-gas accumulation chamber approach (Appendix B). The measurement unit,
316 a Dräger XAM 8000 handheld Multigas device, was equipped with 6 sensors measuring CO_2, CH_4, SO_2, H_2S, H_2, and $O2$
317 simultaneously of which CO_2, SO_2, and H_2S are considered here. The simplified accumulation chamber approach was an
318 adaption as a consequence of uncertainties encountered in previous multi-gas measurement campaigns. Due to different sensor
319 reaction times for ascending and especially descending gas concentrations, the comparison of direct sensor readings might
320 lead to odd gas ratios with an artificial shift towards magmatic components. For that reason, we use the slope of the ascending
321 gas concentration within a defined volume as quantification for a relative surface flow. More detailed information about the
322 gas measurement approach is provided in the supplementary materials. Note that the aim of the gas measurements was not to
323 provide accurate flux estimates but to highlight the spatial variability of the gas flow of certain gas species from the surface.

324 **4 Results**

325 **4.1 Thermal- and optical anomaly patterns reveal the degassing and hydrothermal alteration structures**

326 Degassing and hydrothermal alteration at La Fossa as seen in drone imagery can be traced by mainly two effects.
327 1) The transition from unaltered to hydrothermally altered surface can be traced by a general color shift in the drone images
328 from reddish to grayish (Figures 2A and 4A). This allowed us to constrain a distinct ~70,000 m² sized area surrounding the
329 fumarole field in a circumferential manner. This area is hereafter referred to as the Alteration Zone (ALTZ in Figure 4A/B),
330 and represents the maximum extent of at-surface observable alteration effects that can be associated with the fumarole field.
331 It includes effects ranging from weak surface alteration to strong alteration with intense surface bleaching and remineralization,
332 to complete destruction of the host material. The extent of the ALTZ exceeds the area covered by the high-temperature
333 fumarole (HTF) site by ~50 times (Figure 4A/B), indicating the widespread influence of diffuse degassing and alteration
334 processes.

335 2) Within the ALTZ we observe a segmentation characterized by brightness and color variability expressed in different shades
336 of gray (Figure 4A), the second optical effect, indicating local alteration gradients. Analyzing the ALTZ for this spectral
337 variability by PCA and image classification we can constrain pixels of low-, increased-, or intense surface bleaching and
338 alteration (light blue, dark blue, and red pixels in Figure 4B) and define an alteration index represented by 4 surface Types (1-
339 4), of which Type 1 is the most altered and Type 4 the least altered surface.

Type 1 surfaces are bright grayish intensely bleached surfaces or sulfuric deposits and represent the strongest alteration end members that we can detect optically from our data. Type 1 mainly resembles the fumarole sites and surrounding areas (Figure 4 A/B) but also larger isolated regions that can not be associated with major vent systems. With increasing distance to the degassing centers, we observe a shift towards darker grey (Type 2) and brownish (Type 3) surface colors. **Type 2** is characterized by a gray but comparatively less bright coloring. It typically occurs at the boundaries between Type 1 and Type 3 regions and largely surrounds Type 1 areas, but it also forms several isolated clusters typically embedded in Type 3 areas (units b,d,g in Figure 4). Type 3 is generally darker and more reddish in color, similar to the unaltered parts of the crater surface, but can be well distinguished from the unaltered surfaces by PCA. It makes up ~50 % of the ALTZ and dominates in the central northern and the southeastern parts. Type 4 is a reddish, apparently oxidized surface that dominates the La Fossa cone surrounding the ALTZ.

The surfaces within the ALTZ are generally mixed and composed of more than one type. The ALTZ is characterized by a generally high density of Type 3 pixels, with locally high densities of Type 1 and Type 2 pixels, which then become the dominant surface Type and form larger spatial units, indicating locally higher alteration gradients or larger structural units (units a-g in Figure 4 and details in Appendix C). The largest of these units cover several thousand square meters each.

The thermally active surface (Figure 4C) can be divided into high-temperature fumaroles (HTF in Figure 4D) and diffuse thermally active surface (green pixels in Figure 4D). HTFs are the visible part of the activity that can be constrained by the naked eye in the field, while the diffuse thermally active surface is largely imperceptible. The thermally active surface largely mirrors the alteration pattern observed in the optical data. An analysis of the temperatures obtained at all pixels of Type 1 to 4 surface shows a general increase of mean pixel temperatures from Type 4 to Type 1 surface by an average of 2 degrees (Figure 5). In particular, areas dominated by Type 1 and 2 surfaces reflect the thermal structure well while areas of Type 3 dominance largely coincide with low-temperature surfaces (Figure 4 B/D). An additional Spearman correlation test, applied to the classified surface (32 classes unsupervised, for comparison see Appendix A) and the thermal data (in °C) shows a moderate positive correlation between optical and thermal anomalies (Appendix D). This shows that the detected optical anomalies are meaningful and that degassing and alteration variability occurs even at local scales and can be traced in our close-range drone remote sensing data.

The spatial coincidence of both optical and thermal anomalies highlights the relationship between variations in the surface coloration, caused by alteration processes, and the ongoing influence of diffuse gas flow. A general coincidence of increasing brightness (simultaneously increasing the RGB values) with increasing surface temperature of an area can be constrained (Figure 5).

4.2 Anomaly structure identified from optical and thermal data

The optical and thermal anomalies form distinct spatial units of alteration and elevated surface temperature (units a-g in Figure 4D), which now allow us to infer the following surface structure of the fumarole field and its wider field of activity.

The centers of degassing activity are high-temperature fumaroles (HTF). These are the "visible" parts of the activity that can be perceived in the field (red pixels in Figure 4D). We spatially constrain the HTFs based on apparent temperature values with T > 40 °C in our 150 m overflight data. Using this as a threshold we find that the HTFs cover an area of 1223 m², and occur exclusively in the Type 1 surface. However, HTFs represent only a fraction of the active surface.

The total extent of the surface that has to be considered active is much larger. The surface with elevated temperature covers ~30000 m² (green pixels in Figure 4D, T > 22 °C or 5 °C above the background), exceeding the area covered by HTF by a factor of 25. The surface that is considered hydrothermally altered (ALTZ ~70,000 m²) exceeds the area covered by HTF by a factor of ~60, highlighting the widespread influence of diffuse degassing and alteration processes.

Besides the HTF we have constrained larger units of elevated surface bleaching and surface temperatures that can be considered structurally important and centers of diffuse degassing activity.

Units a and b are diffuse features of increased surface bleaching (Type 1 and 2) and surface temperature, embedded in the Type 3 surface and surrounding the eastern fumarole field in the form of an aureole shape. Neither can be associated with major vents. The observed maximum surface temperature for unit a is 43.7°C (0.43 m resolution) and the average temperature is 25°C, ~8°C above the background. It is located at a distance of 25 to 50 m downslope from the eastern rim fumarole complexes, separated by a low-temperature zone (LTZ). Unit b, the southern part of the aureole is a 120 m long and 20 - 35 m wide anomaly located subparallel on the inner side of the crater. It extends over ~2100 m² and has a maximum surface temperature of 46°C and an average temperature of 26°C (9°C above the background). The temperature range and spatial extent of units a and b are comparable. In the field, both are difficult to identify as there is little or no evidence of degassing (Appendix E). Like unit a, unit b is also separated from the main fumarole vents by the LTZ. Its northern boundary corresponds exactly to the positions and curvature of the fumarole alignments at a relatively constant distance of 30 meters. In unit b, we observe a temperature gradient with higher temperatures at greater distances from the fumarole vents and an apparently more active center in the southeastern corner. Another thermal anomaly with a similar shape and orientation is located further south inside the crater.

Units d and f are similar aureole-like features in the western fumarole field, associated with fumarole complex F0. They circumferentially surround fumarole complex F0 at a distance of 5 to 15 m, also separated from the HTF by a Low-Temperature Zone (LTZ), but to a lesser extent than that observed for units a and b of the eastern fumarole field. The southwestern section of this aureole, unit d, appears as a larger heated complex with stronger surface bleaching (Type 1) and higher temperature (mean T=27°C), and a temperature gradient with higher temperatures further away from the major fumarole complex. The boundary to the low-temperature zone is sharp with a sudden drop in temperature of 10 to 20°C and a strong associated color shift (Appendix C). The aureoles of F0 and F11 have in common that they are encircled by a network of polygonal net-shaped thermal anomalies in the far field.

Low-temperature zones (LTZs) dominate the central parts of the fumarole field. The LTZ have only slightly elevated temperatures relative to the background (18-21°C or 1-4°C above background) and can be optically constrained by a darker Type 3 surface coloration. From field observations, we have concluded that these LTZ form a strong, apparently sealed surface complex. Therefore LTZ might indicate largely sealed sections of the fumarole field which inhibit gas flow at the surface. The 3 central LTZ1-3 (Figure 4D) cover an area of ~12,000 m².

Unit c is a broad complex of highly altered material (Type 1) and significantly high surface temperatures. It is potentially the most altered member in the central crater region. It covers an area of ~8000 m² and the maximum and average apparent temperatures observed are 87°C and 29°C. It is associated with the HTF FA and F58. Considering the thermal structure of unit c, it is a heterogeneous unit formed by a network of higher temperature anomalies embedded in lower but, with respect to the background, significantly increased tempered surface. This area is associated with the northwestern crater unit, which is the most recent explosion crater.

Unit d is an area of diffuse activity associated with the inner crater part of fumarole complex F0, showing a significant shift in surface colorization and temperature, some 20 m away from the fumarole complex. The boundary is distinct and visible to the naked eye (Type 3 to Type 1). The temperature shift is on the order > 20 °C.

Unit e is a large branching thermal and optical anomaly of the upper fumarole field. It can be constrained by its gray coloration embedded in the reddish unaltered surface and also by its increased surface temperature. It is a 120 to 150-m-long branch-shaped network of anomalies on the inner crater wall. The central feature is oriented E-W and located ~ 20 m south and below the helicopter platform and the crater rim. We constrained its size to ~2500 m² (only the western branch, without intersection to unit d) and the recorded maximum and average apparent temperatures are 45.0°C and 25.9°C respectively. Some smaller clusters of localized degassing, alteration, and increased surface temperature, visible at the surface by its bright coloration, are observed in the northern section of the fumarole field (unit g) towards La Forgia.

4.3 Ground truthing - verification of observed anomalies

We have carried out mineralogical (X-ray diffraction) and geochemical (X-ray fluorescence) analyses of bulk rock samples collected at representative locations and surface degassing measurements. The aim is to verify the observed anomaly pattern of alteration gradients and distinct active units and to investigate the relationship between the optical and thermal anomaly pattern and modern degassing and hydrothermal alteration processes. In this way, we provide ground truthing and demonstrate that the anomalies observed are significant.

4.3.1 Present-day surface degassing pattern

The measurements of diffuse degassing from the surface allow us to compare the present-day surface degassing pattern to the observed optical and thermal anomalies (Figure 6 A/B). We performed surface degassing measurements of CO_2, H_2S, and SO_2 simultaneously in the diffuse degassing regime at 200 measurement points (~100 points within and outside the ALTZ) throughout the whole northern crater section (details of gas measurements in Appendix B).

The observed relative flux values for CO_2 range from 0 to ~9000 ppmv/s with an average of ~900 ppmv/s. They are considerably higher (x*10³) than the SO_2 and H_2S flux at the respective locations. For both, SO_2 and H_2S a maximum gas flux of < 10 ppmv/s was measured and the average is below 0.5 ppmv/s.

Looking at the spatial distribution of the measured gasses we observed generally higher gas levels within the alteration zone ALTZ and at the ALTZ boundary, for each of the measured gas (Figure 6 C/D). The average CO_2 flux is 660 ppmv/s outside the ALTZ and 923 ppmv/s within the ALTZ. Thus, the averaged CO_2 flux inside the ALTZ is about 1.4 times higher than outside but is particularly high in some of the constrained units a-g. However, the CO_2 flux has a wide spatial distribution and high flux values of above 2000 ppmv/s can also be observed outside the ALTZ and at a distance to the ALTZ boundary (Figure 6 A/C).

SO_2 and H_2S in contrast appear spatially more strongly confined, and significant flux values can be exclusively observed within the ALTZ (Figure 6 B/D). Values for SO_2 and H_2S inside the ALTZ exceed the outside-ALTZ values by 13 and 15 times. This higher diffuse flux, although at average low concentrations, might promote a surficial process of chemical weathering and surface bleaching, potentially causing the observed color shift from a reddish-oxidized surface toward gray and will be discussed further based on analyses of the geochemical composition of rock samples in Chapter 5.2.

Comparing the surface degassing to the observed optical and thermal anomaly pattern (Figure 6 E-G), we see that high values were observed especially in units a or b on the eastern side of the fumarole field, coincident with increased alteration (Type 1 and 2) and thermally active surface, followed by other constrained units c-g. However, the strongly bleached and apparently highly altered unit c shows, other than expected, rather small gas fluxes, although its surface temperature is significantly increased with respect to other identified units. This might indicate reduced surface permeability and surface sealing processes and will be discussed in Chapter 5.3.

While SO_2 or H_2S flux values for Type 1 and 2 surfaces are increased, only low fluxes were constrained for the Type 3 surface and no flux for the unaltered surface (un in Figure 6 E-G). Note that the central sections of the fumarole field were not sampled due to the close vicinity to HTF and expected high flux values. The data shown here is only representative for the diffuse degassing domain.

4.3.2 Mineralogical composition of the alteration gradients

XRD Analysis was performed along two transects A and B, and XRF analysis was performed on samples taken along three transects A-C (Figure 7), crossing postulated alteration gradients.

Transect A crosses from the unaltered surface over Type 3 into the Type 1 surface (T3-T1 boundary in Figure 7) of the highly altered unit c. Transect B is oriented along the HTF on the crater rim in an east-west orientation from Type 1 surface into the LTZ (Type 3). Transect C crosses the eastern fumarole field from the unaltered surface, through the Type 1 and 2 surfaces in unit B, the LTZ (Type 3) on both sides of the HTF, to Type 1 and 2 surfaces, and eventually the unaltered material outside the ALTZ. This transect represents the variability in the rather diffuse degassing regime as no samples close to the HTF were used for the analysis.

471 Results of all samples support local alteration gradients within the ALTZ and show significant changes in the mineralogical

472 and geochemical compositions (Table of XRD results in Appendix F). The dominant mineral phases observed in samples of

473 transects A and B are sanidine, cristobalite, and elemental sulfur (Figure 7). Additionally, most samples contain amorphous

474 material, representing glassy phases typical for volcanic sequences. For comparability, mineralogical concentrations refer to

475 the crystalline phase, while amorphous contents are stated with respect to the total. Note, however, that bulk rock geochemistry

476 refers to both phases and cannot analytically distinguish between amorphous and crystalline.

477 Considering compositional changes along transect A we observe a high proportion of sanidine feldspar and lesser cristobalite

478 in the relatively unaltered samples (Type 4). With an increasing degree of alteration, we observe a general loss of cristobalite

479 and sanidine while sulfur contents increase (Figure 7). Samples from the unaltered reddish Type 4 surface (A1) outside the

480 ALTZ and Type 3 surface (A2/3) inside the ALTZ are similar in composition and show high sanidine and cristobalite contents

481 of 86-87 % and 13-14 % in the crystalline part, respectively, yet low to no sulfur contents. These samples were taken in areas

482 of no or only slightly increased surface temperatures of < 22 °C (i.e. < 5 °C above the background). Samples A4-6 are taken

483 in unit c, a complex of high alteration and increased mean surface temperatures of 28°C (~10°C above background). In this

484 strongly altered unit, cristobalite is absent, along with a decrease in sanidine to 60-70 % relative to the least altered samples

485 and an increase in sulfur contents of up to 20-40 % in the crystalline portion of the rock sample. However, the amorphous

486 components constitute a high proportion of these sample(s), showing ca. 50 % in samples A6 and B1.

487 Samples taken on the upper rim along transect B in the high-temperature fumarole regime (V-AHT) contain total sulfur

488 contents of 50 to 100 %, while cristobalite is absent in these samples. Sample B3, a piece of grayish crust is taken from LTZ3

489 (~21°C, 4°C above background) in between the high-temperature fumaroles F0 and F5 and contains 100 % sulfur, highlighting

490 the precipitation and sealing potential of degassing activity at the surface.

491 Comparing the changes of surface coloration with changes in the mineralogical composition we can constrain no significant

492 effect at the ALTZ boundary, i.e., the transition from unaltered to altered surface (A1-A2/3), although the optical effect is

493 major. However, significant compositional changes, e.g. the complete loss of cristobalite and increasing sulfur content are

494 observed at the ALT - AMT boundary (blue mark in Fig. 6), coincident with the shift from Type 3 to Type 1 surface into unit

495 c.

496

497 **4.3.3 Bulk geochemical composition of the alteration gradients**

498 For samples without amorphous fraction, bulk geochemical composition correlates reasonably well with mineralogy

499 determined by XRD, assuming ideal stoichiometry. The difference between theoretical bulk composition and true composition

500 is within 10 % of the respective element, which we consider a good estimate given sample heterogeneity. Only for sample A5,

501 the high Mn content remains unmatched by XRD analysis. Subtracting the theoretical bulk composition of the crystalline

502 fraction from the true bulk composition, we can thus estimate the chemical composition of the amorphous fraction. The

503 amorphous fraction is similar to the crystalline counterpart mainly composed of SiO_2 and some minor (< 5 wt%) phases, as

well as elevated Mn contents. The high Mn contents were only observed in samples with medium alteration and elevated temperatures, both in samples with and without a significant contribution portion of amorphous material. It is thus likely that Mn is contained in the crystalline phase, yet could not be detected due to the high SiO_2 signals derived from sanidine and amorphous material.

The bulk geochemical composition (Figure 7 and data table in Appendix G) agrees with the mineralogical composition. All samples are high in SiO_2 content and, therefore, can be considered to belong to the large silicic-alteration complex earlier described by Fulignati et al. (1999). The samples show a slight variability of SiO_2 between 67-82 wt. % and plot on the rhyolite field within the TAS diagram (Middlemost, 1994; not shown here). The amorphous component, typical for rhyolite, consists of mainly SiO_2, with minor amounts of Fe and Al, based on the difference between the theoretical and actual geochemical composition calculated from stoichiometric mineralogy. Three samples also have significant MnO, possibly caused by hydrothermal leaching and precipitation as amorphous crusts. However, the variability of MnO will not be detailed further in this study.

Dominant in transect A is the loss of Al_2O_3 from the unaltered Type 4 surface (> 10 wt.%) outside ALTZ to the Type 1 surface of the highly altered unit c (< 0.4 wt.%). Similarly, Fe_2O_3 is decreasing from an average of 1.6 to 0.3 wt.%. The loss of Al_2O_3 and Fe_2O_3 is likely related to the alteration of sanidine and the elution of iron- and aluminum-sulfates formed due to the contact with sulfuric gas. The most significant changes occur, similar as observed in the mineralogy, not at the transition from unaltered to altered (ALTZ-boundary) but at the T3-T1 boundary (blue line in Figure 7) at the transition from Type 3 to Type 1 surface. Transect C crosses from the unaltered surface through unit a, the northern LTZ, the southern LTZ, unit b, Type 3 surface, and eventually the unaltered surface. Compositional changes from unaltered (Type 4) to altered (Type 1 and 2) surface of units a and b, here, are minor with relatively stable values for Al_2O_3 (6-12 %), Fe_2O_3 (1-3 %), TiO_2 (< 0.5) and Mn (~0). At the transition from active units a and b (Type 1 and 2 surface) to the LTZ (Type 3), we observe a significant increase of sulfur content from < 2 % to 12-40 %. However, this increasing sulfur content here is not coincident with the systematically brighter surface color observed for other altered units. LTZ show the same rather dark surface observed for Type 3 surface elsewhere, which is a discrepancy to the effects observed in the western fumarole field and indicates that LTZ have to be considered subject to different surficial processes. This will be discussed in Chapter 5.3.

5 Discussion

Various studies have previously explored the geochemistry (e.g. Fulignati et al., 1999), petrology (e.g. De Astis et al., 1997), geophysics (e.g. Revil et al., 2008) and remote sensing signal (e.g. Mannini et al., 2019; Coppola et al., 2022) of the La Fossa crater, Vulcano island. In this study, we combine close-range remote sensing, image analysis, mineralogical and geochemical

analyses of rock samples, and the study of the present-day surface degassing of the La Fossa crater and analyse the surface expression of hydrothermal activity. Through this combination of ultra high resolution (< 10 cm) drone image analysis with mineralogical/geochemical analysis, we are able to provide a holistic picture of the surface degassing and hydrothermal alteration pattern, highlighting an aureole-like organisation of the alteration field that distinguishes distinct units that grade from inner high-temperature fumaroles to sealed surfaces (LTZ) and to diffuse degassing areas at a greater distance. An area of approximately 70,000 m², which we have termed the Alteration Zone (ALTZ), outlines the maximum extent of observable alteration effects and highlights that degassing and alteration can be traced well beyond the central high-temperature fumarole activity sites (HTF). The ALTZ is similar to the diffuse flux zone previously identified by Mannini et al. (2019), and is in fact ~50 times larger than the area covered by the high-temperature fumarole domain. However, from the optical data, we observe further variability within this zone expressed in active units a-g, which also coincide with the diffuse thermal activity and cover 25 times the extent of HTF. Here we can further detail the surface structures and activity patterns identified in previous works, (e.g. Harris et al., 2009; Mannini et al., 2019) which divide the active region into a vent flux zone and a diffuse flux zone. In particular, we can further detail the vent flux zone by outlining high-temperature fumarole locations based on high-temperature pixels. We further show that thermal radiation and gas flux of the ALTZ or diffuse flux zone are not uniform but show strong local variability, with high fluxes in identified active units a-g and low fluxes in larger parts of the central fumarole field associated with LTZ (Low-Temperature Zones) or the unaltered regime.

Although the structural study is based solely on drone-derived imagery and thermal infrared data, our detailed observations of local activity and alteration gradients are supported by variations in mineralogical and bulk geochemical compositions of representative rock samples. Although we have performed a classification of the image data in this work, already visual observations can show a general shift from reddish to gray surface color, which coincides with areas of increased diffuse gas flow. Such color anomalies can therefore be used as guide in the field. A variability in surface brightness and gray hues coincides with alteration gradients and major active units, and the congruent optical and thermal anomaly pattern indicate the link between surface coloration and degassing-induced alteration processes. This relationship underlines the potential of the presented combination of methods as an efficient first-order site investigation tool for volcanic degassing and alteration systems that can be applied to volcanoes elsewhere.

5.1 Alteration Zone (ALTZ) controlled by sulfuric gases and elution processes

The ALTZ is characterized by a surface color shift from reddish to gray and coincides with higher SO_2/H_2S flux and appears to represent a zone of diffuse acid gas flow (Figure 4). All measurements with a significant flow of sulfuric gas species are from inside the ALTZ, while the flux of CO_2 was high well beyond the ALTZ. We, therefore, suggest the general color shift from reddish to gray to be related to a higher flux of sulfuric gases, promoting chemical leaching of iron oxides via the reduction of the initially contained iron oxides to iron sulfates, which are strongly soluble in rain or in condensing water vapor and are

thus prone to rapid elution. Iron oxide content in our analyzed samples ranges from 1.5 % (sample A1) in the unaltered regime, to 1.1-1.4 % for A2/3 samples, and to 0.3 for samples of the highly altered unit c (sample A4-6). There is a gradual reduction following the postulated alteration gradient, with the strongest changes along the T3-T1 boundary (blue line in Figure 7). The 1.5 % Fe_2O_3 for our rock sample of the unaltered regime is a rather low value and might be related to the fact that the sample was taken very close to the ALTZ boundary. It consists of > 50 % amorphous material. Fulignati et al. (1999), who provide a broader sampling database estimated Fe_2O_3 contents of unaltered 1888-1890-eruptive products with 2.5-6.7 %, which reduces to an average value of below 1 % in the silicic-alteration regime (Fulignati et al., 1998; Fulignati et al., 1999; Boyce et al., 2007).

Further evidence for chemical leaching is found on the crater floor, where deposits form a colored layer resembling the color spectra widely observed on La Fossa, with bright reddish deposits close to the fumarole field resembling fluvial patterns. We believe that the optically anomalous gray surface at Vulcano can generally be used to infer areas of present higher acid gas flux or former discharge of acid gases. Analyzing the broader area of the central crater region, we can infer multiple other areas where we observe similar changes of colorization that indicate similar argillic or strong silicic alteration effects at the surface. These are located on the southern inner crater, the outer crater rims, the 1988 landslide area (Madonia et al. 2019) and the northern flank towards Vulcano Porto. These zones of strong alteration are indicated in red in Figure 1B or Müller et al. (2021).

5.2 Alteration gradients on local scales

With average high SiO_2 contents of > 70 %, the sampled areas correspond to the large silicic alteration complex suggested by Fulignati et al. (1999), Azzarini et al. (2001), Boyce et al. (2007), and others. In our study, we show evidence for strong local alteration gradients and structurally important units and spatially constrain them, thus we complement earlier studies.

Color shifts observed within the ALTZ associated with units a-g (brightness effects, hues of gray) are likely controlled by the degree of hydrothermal alteration, secondary mineral formation, and especially sulfur content in the respective surface samples. Coincident with characteristic changes in the surface coloration from Type 4 towards stronger bleached surfaces of Type 1, we observe a relative decrease of the initial mineral and element composition and a simultaneous increase in sulfur content for most of the obtained samples (Figure 7). While sulfur content in Type 1 surface ranges from 6 to 31 %, for Type 2 it is already below 2 %, and for the unaltered fraction, it is below 0.2 %. We can, therefore, confirm a general link between alteration gradients, sulfur contents, and surface brightness (or surface types) in our remote sensing data (Figure 8).

An exception from this trend are sulfur contents of the Type 3 surface. Here we observe two distinct clusters (Figure 8), one with values below 0.5 % and one with extraordinarily high sulfur contents of 12 to > 60 %, both showing a similar surface coloration. All Type 3 samples with high sulfur contents are exclusively taken from LTZ. This strong discrepancy of sulfur content and surface coloration within the low-temperature zones suggests next to alteration gradients also surficial or shallow processes of mineral deposition and formation of sulfur-rich encrustations that form sealed surfaces, especially in the near field

600 of fumaroles. The low temperatures observed within LTZ and the limited surface degassing highlight the efficiency of such

601 sealing processes. So far we can not distinguish LTZ from Type 3 surfaces in our optical data (Figure 8). A distinction,

602 however, would be beneficial as it would provide a method allowing for the precise spatial constraint of sealed surfaces from

603 simple UAS-derived RGB imagery.

604 The intensity of optical and thermal effects and associated changes in mineralogical and chemical composition, and degassing

605 are not always equally significant. Although the general shift from unaltered surface to altered surface (ALTZ-boundary, shift

606 reddish to gray) is a major criterion for the identification of degassing and alteration extent in our data, the associated changes

607 in compositions are minor (Figure 9). The larger changes are observed within the ALTZ at the T3-T1 boundary (Figure 7).

608 Here we observe a sudden decrease in the initial mineral and bulk geochemical composition and an increasing sulfur content.

609 We interpret the rather low changes at the transition from unaltered to altered at the ALTZ boundary to be related to rather

610 weak or surficial alteration effects. The size of obtained samples was on the order of ~2000 cm², including the surficial part,

611 but extends down to ca. 10 cm depth. This way, it was not possible to trace mineralogical or geochemical changes at the surface

612 only. The samples obtained at the T3-T1 boundary, on the other hand, show strong changes and reveal the general systematics

613 of alteration effects, especially those samples taken in unit c, which might be considered one of the strongest alteration end

614 members of the central crater region.

615 The identified surface patterns with respect to alteration gradients and structural units result from long-term evolution.

616 However, some features may be subject to rapid changes. During the volcanic crisis in 2021, we observed, for instance, the

617 formation of a new fumarole complex, which will locally change the composition, sulfur content, and surface type considered

618 (cf. Figure 11), as is the case with sulfur deposits at the surface that can change quickly due to rainfall.

619

5.3 Heat budget - evidence for diffuse activity and surface sealing

621 Heat budgets on Vulcano have been studied earlier by e.g. ground-based surveys or satellite data (Chiodini et al., 2005; Harris

622 et al., 2009), providing a range of estimates of thermal emissions (Mannini et al., 2019; Silvestri et al., 2019; Coppola et al.,

623 2022). We compare our results to those using a remote sensing approach. Mannini et al. (2019) outlined a diffuse flux zone,

624 which is comparable to the ALTZ defined by us. Further, they divided this zone into a diffuse flux zone and a vent flux zone

625 and estimated the thermal radiation.

626 We outlined the surface structure of the degassing and alteration system (simplified in Figure 10 and detailed views of the

627 different alteration and thermal units in Appendix C) based on the detection and classification of optical and thermal anomalies

628 supported by additional mineralogical, geochemical, and degassing information, and spatially constrained high-temperature

629 fumaroles (HTF), major diffuse active units a-g, and Low-Temperature Zones (LTZ). We quantified their importance for the

630 degassing and alteration system by calculating their thermal energy release according to the Boltzmann Law (Eq2 and Figure

631 10) for both, anomalies with T > 22°C, and identified units based on a spatial constraint, also including values < 22°C.

632 Therefore our identified structure differs from the vent flux and diffuse flux zone shown by Mannini et al. (2019).

High-temperature fumaroles in our study have average radiant exitance values of 82 W/m² but can only account for 28 % of the total emitted thermal energy (calculations based on pixels with T > 22°C and a corrected background of T = 16.71°C). Note that when considering pixels with T > 40°C (as outlined by red patches in Figure 4D) the cumulative radiation of HTF would decrease to 0.2 MW only and the radiant exitance would increase to 242 W/m². The rest is released by the diffuse degassing part of the system. Although a direct comparison may be difficult, due to different outlines chosen for the respective flux zones, different sensor systems, and different background correction values, our cumulative radiation (Rcum in Figure 10) for the HTF is comparable to those of Mannini et al. (2019). These authors suggested a vent zone heat flux of 0.35-0.96 MW. Our estimate was ~1 MW, of which 0.5 MW are contributed by the high-temperature fumarole vents and 0.52 MW by unit c. This is also in accordance with the findings of Coppola et al. (2022), who estimate a similar vent zone flux from VIIRS imaging bands.

However, the contribution of the diffuse thermal regime approximated by us is lower compared to estimates in other studies (e.g Mannini et al., 2019), which place the contribution of the diffuse flux zone (comparable to our ALTZ) on the order of 90 % of the total flux. This is likely related to the fact that we did not estimate the flux of the ALTZ in total, but of multiple larger anomaly units within the ALTZ that have apparent structural importance for the degassing system and contribute ~50 % to the total flux. For future studies, a distinction into 3 different thermal regimes, a vent flux / high-temperature fumarole zone, a diffuse active units (like a-g shown in this study), and a broader low-temperature anomaly field (diffuse flux zone/ ALTZ) may be recommended to better resolve close range thermal-infrared remote sensing information with data from satellite-based studies.

Regarding the heat budget estimated by us, the most dominant diffuse unit in terms of thermal energy release is unit c. It has the second-highest average radiant exitance of 76 W/m² and exceeds, with 29 % of the total thermal radiation, the cumulative radiation of the HTF. Unit c is not only a highly altered complex with the strongest bleached surface and increased surface temperatures, there is also a discrepancy to the current degassing activity. Relative gas flux values measured within unit c are lower than observed for units a and b, for instance. This phenomenon might be a consequence of the permeability reduction or sealing processes due to the more advanced hydrothermal alteration (cf. Heap et al. 2019). This proposition is supported by the strongest changes in mineralogical and bulk geochemical composition observed in our samples, implying mineral (re-)precipitation is a major process in this particular unit.

Diffuse aureoles (unit a/b) on the eastern side of the fumarole field cover several thousand m² each, more than the area covered by HTF. The diffuse aureoles contribute 6 to 7 % each to the total thermal energy release, equivalent to 25 % of the energy emitted in the high-temperature zone (HTF + unit c). Their bleached surface, increased surface temperatures (Figure 4), and higher gas flux values (Figure 6 E-G) highlight their importance for the surface gas-drainage capability. However, mineralogical and bulk-chemical data suggests that the degree of alteration is less in these units, compared to unit c. This observation suggests that these sections are younger and therefore less altered and highlights their importance for the present-day degassing system.

Units d and e are large diffuse degasing domains of the western fumarole field of which unit d is a part of the thermal aureole surrounding F0 and unit e is a ~200 m long branched anomaly, located rim parallel west of F0. Both have a similar contribution to the total thermal energy release as units a and b. Unit d is separated from F0 by a low-temperature zone (LTZ3). The transition from LTZ3 to unit d is sudden and accompanied by a temperature jump of ~ 20°C. The difference in the average temperature between unit d and LTZ3 is on the order of 5°C. Also here we observe apparent surface sealing for the whole central fumarole field. Unit f, the northern section of the F0 aureole, and anomalies in the area north of the fumarole field (unit g) have a minor contribution.

The Low-Temperature Zones (LTZ) 1-3, which separate diffuse aureoles from the HTF, have a Type 3 surface coloration, significantly lower temperatures, and radiant flux and exitance values than the neighboring aureole regions, what indicates processes of surface sealing. Indeed, no gas flux could be constrained for the LTZ of the eastern fumarole field. From field observations and lab analyses (Figure 7), we constrained the LTZ as strong, sulfur-rich surface complexes that effectively seal the surface and inhibit gas escape. The depth of these sealed complexes can not be constrained by our data, but we can approximate the spatial extent. Considering only the 3 LTZs of the central and eastern fumarole field, they cover a total area of ~12000m², which is a significant fraction of the ALTZ. In other words, ~ 20 % of the surface of the ALTZ is apparently sealed, which forces lateral gas flow to the aureole regions. This was proven by observations during the 2021 volcanic crisis at La Fossa. While at fumarole sites and diffuse active units like units a and b showed an increase in mean temperatures and thermal energy release, the radiation within LTZ remained stable and low, highlighting the efficiency of the proposed seal. This was observed for all central LTZs, and is exemplified in a cross-section through the eastern fumarole field section (Figure 11D).

6 Conclusion

Our investigation of the fumarole field of the La Fossa cone allowed us to constrain the degassing and alteration structure, define major, so far undescribed units of activity, and quantify their importance for the degassing system. Such high-resolution studies can greatly contribute to the understanding of structural architecture and add to our understanding of the intrinsic complexities of fumarole fields. This realisation has implications for hydrothermal alteration studies, particularly for the identification of local variability, since local variations are frequently associated with mechanical, chemical, and permeability contrasts. The recognition of such contrasts is of use for an improved assessment of volcanic and degassing activity, but also possibly for other hazard aspects, such as e.g. stability assessments. We anticipate that combined remote sensing and petrological studies will prove beneficial for pre-site reconnaissance surveys for hydrothermal energy exploration, the detection of sampling locations for alteration-related studies, and, importantly, for hazard monitoring of volcanic crater areas and associated risk assessment.

696

7 Tables

Table 1: Overview of the processed data sets that were used for the following analyses. From the optical data, an orthomosaic and DEM were generated covering 3.74 km² with pixel resolutions of 8.6 x 8.6 to 17.3 x 17.3 cm. From the high altitude infrared overflight, an infrared mosaic was acquired covering 3.23 km² with 38 x 38 cm resolution. All data sets cover the complete central section of the La Fossa cone.

Data set	Acquisition date	Pixel resolution in cm	Coverage in km²	Point density in p/m²
2019 orthomosaic	14.11..2019	8.6 x 8.6	3.74	135.20
2019 DEM	14.11.2019	17.3 x 17.3	3.74	33.41
2018 IR mosaic	15.11.2018	38 x 38	3.23	5.64

8 Figures

713
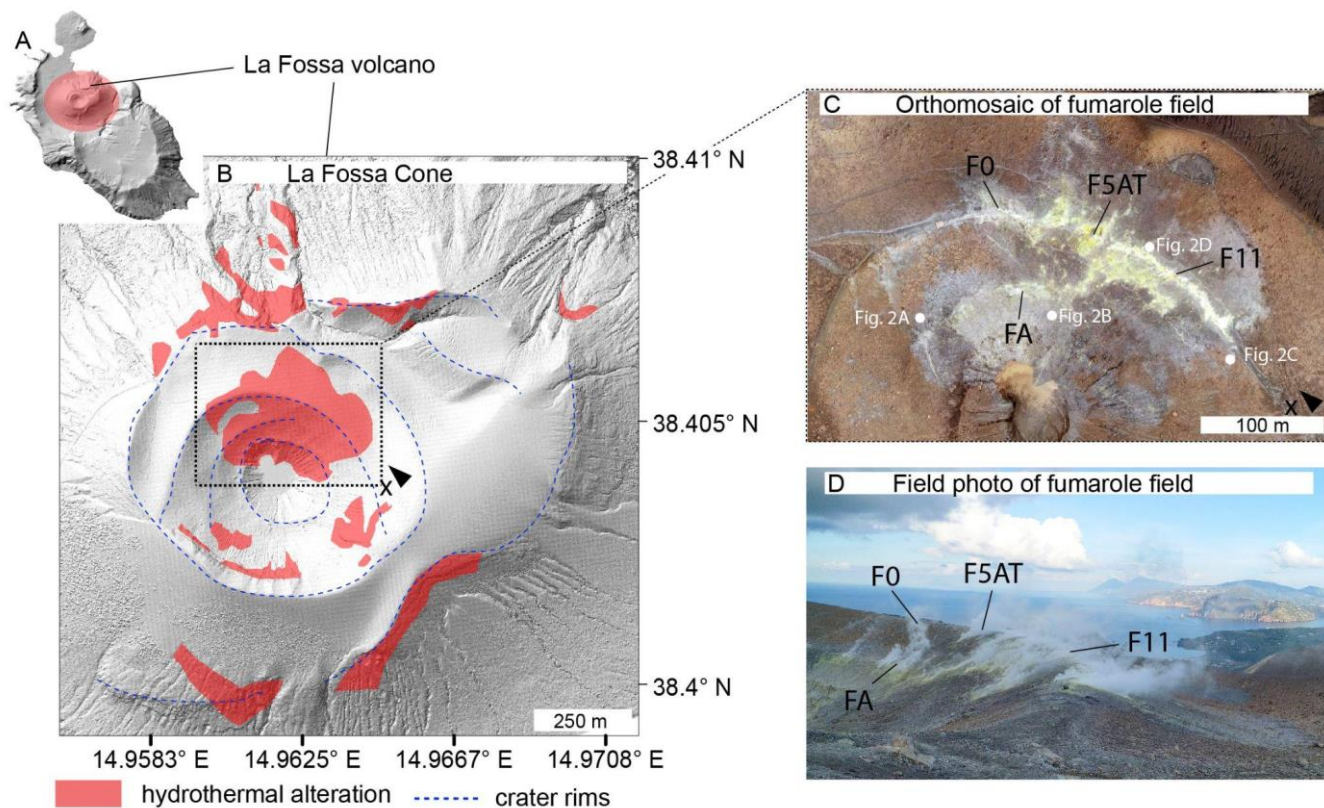
714   Figure 1: Overview of the degassing sites at La Fossa cone, Vulcano Island (Italy). A) Vulcano Island as a shaded relief map.

715   The red circle indicates the location of the La Fossa cone. B) Central summit area of the La Fossa Cone. Blue dashed lines

716   indicate crater rims from different eruptive episodes. Areas of degassing and hydrothermal alteration are highlighted in red

717   following Müller et al. (2021). The dashed box outlines the most prominent center of degassing and alteration, the high-

718   temperature fumarole field. C) Birds-eye view of the high-temperature fumarole field with prominent fumaroles F0, F5AT,

719   F11 and FA marked. The locations of field photographs of Figure 2 are indicated by white dots. D) Field photo of the fumarole

720   field. Location and viewing direction are indicated by an x and an arrow (B/C).

721
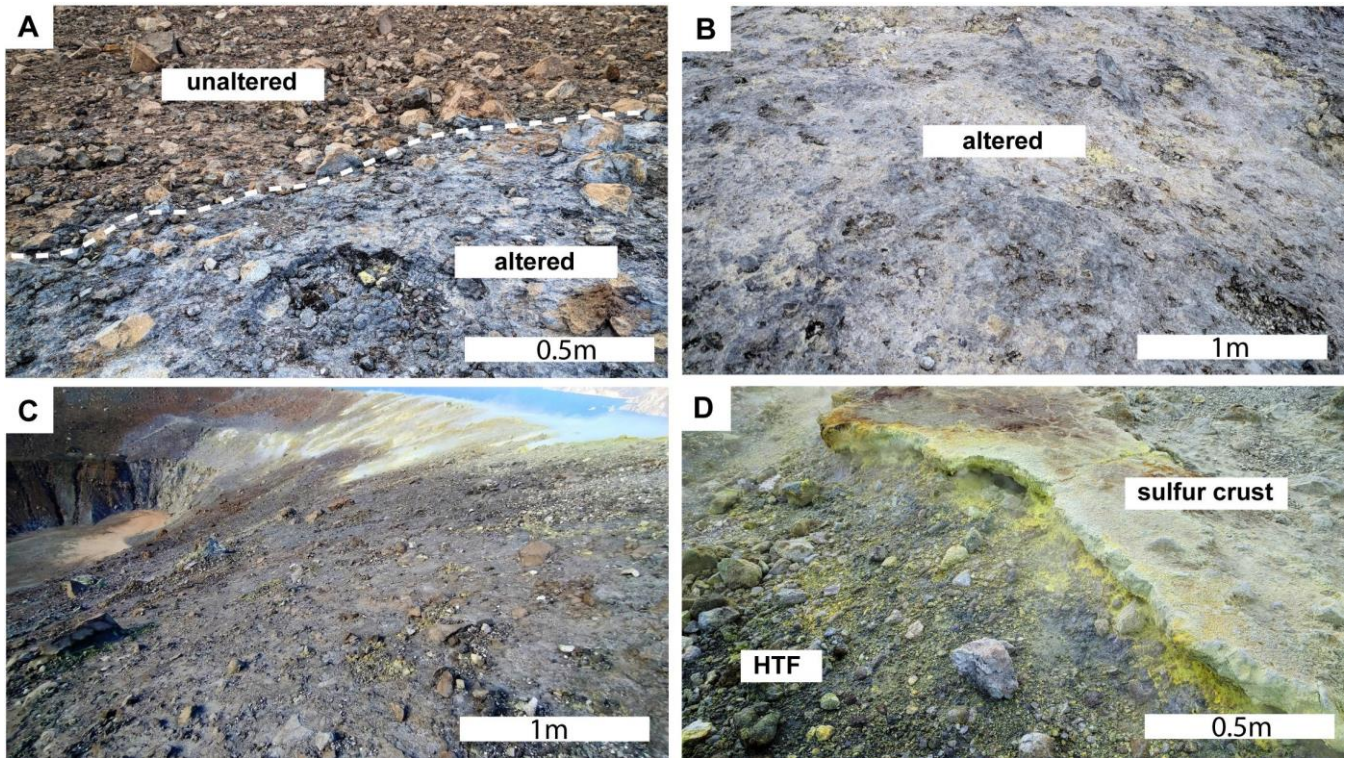
722

723 Figure 2. Different surface types and colorations in the La Fossa cone. A) Transition from unaltered to altered bleached surface.

724 B) Intensely altered and bleached surface. C) View from the east onto sealed surfaces D) High-temperature fumarole (HTF)

725 and deposited sulfur crust.

726
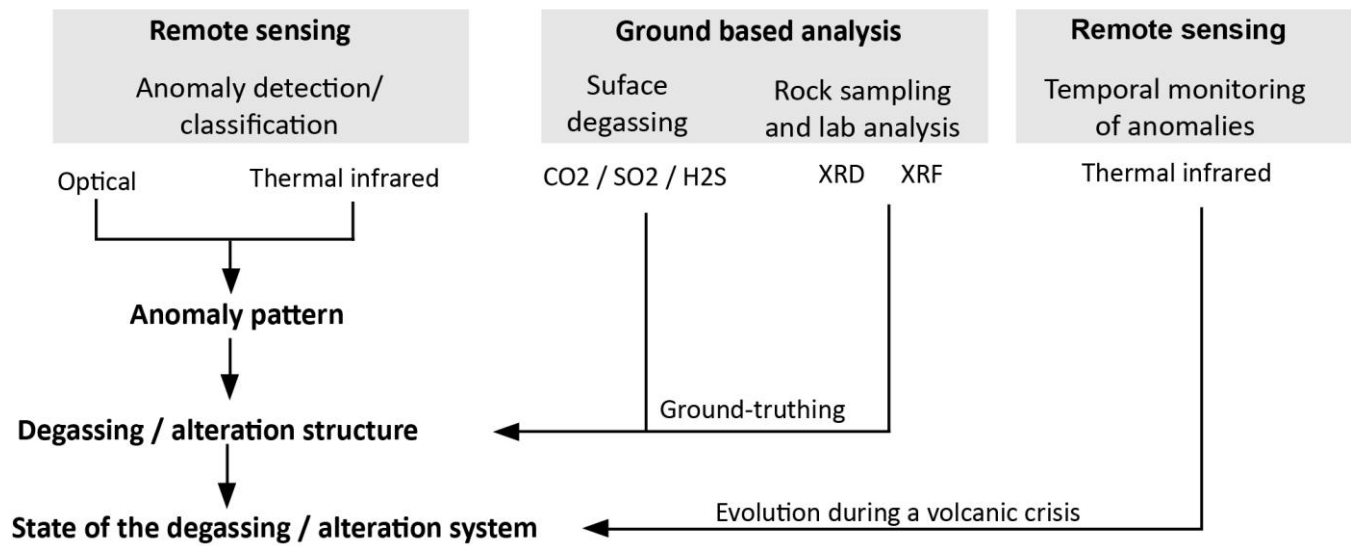
Figure 3: Overview of the general workflow used for this study. An anomaly detection from optical and thermal infrared remote sensing data allows us to reveal the anomaly pattern and infer the surface structure of the degassing and alteration system. To validate the observed structure, the remote sensing study was complemented by surface degassing measurements revealing the present-day degassing pattern, and by X-ray diffraction (XRD) and X-ray fluorescence (XRF) analysis of selected rock samples to prove different alteration units based on changes in mineralogical and bulk-chemical composition. Continuous monitoring by high-resolution thermal remote sensing data allows to record dynamics within the system and to draw conclusions about the general condition of the degassing/alteration units, e.g. with regard to alteration-related processes like surface sealing.

738
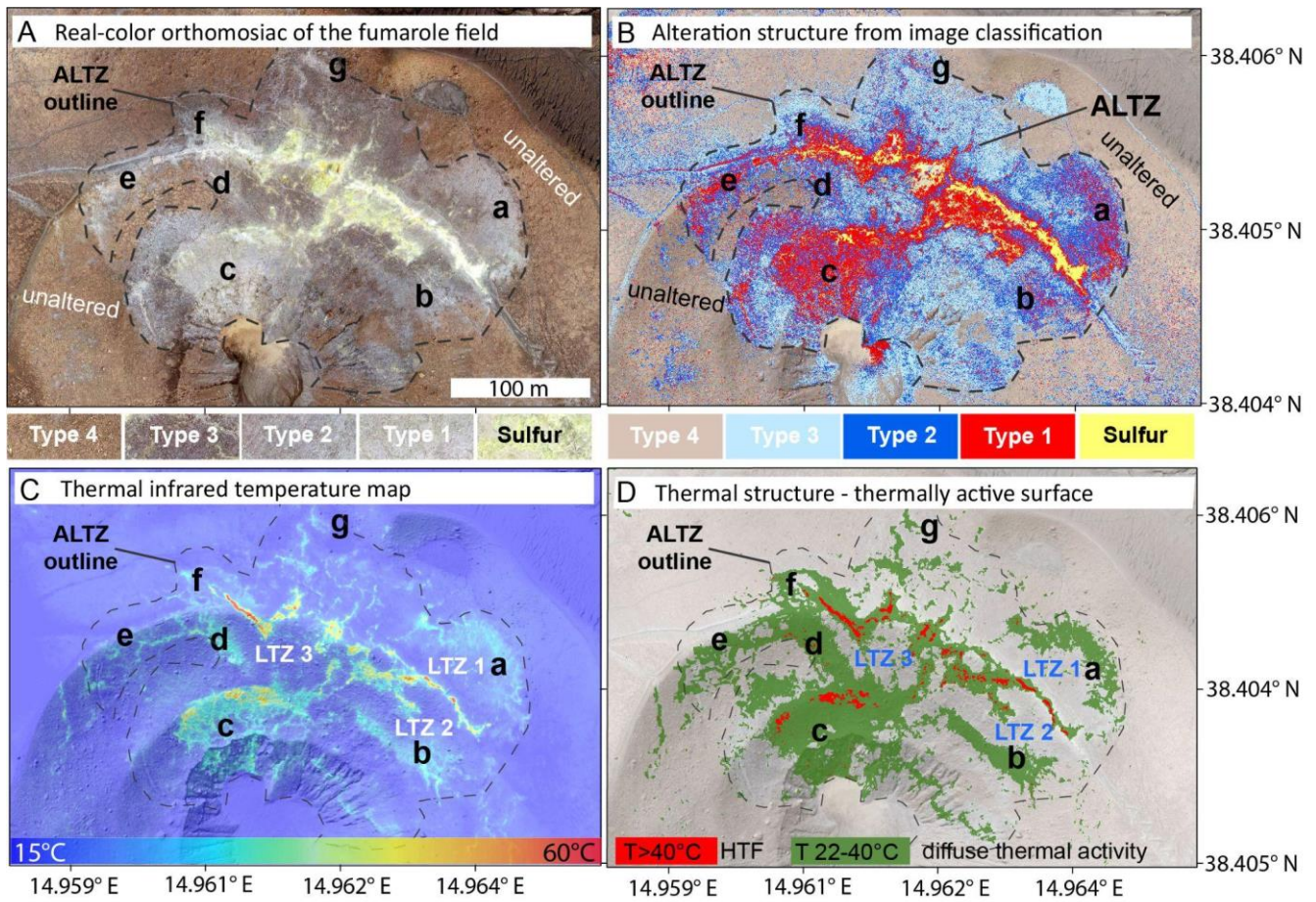
Figure 4: Alteration structure of the La Fossa fumarole field. A) True color image of the high-temperature fumarole field with color samples of the surface types 1-4 and sulfur at the bottom of Fig. A. B) Alteration structure of the fumarole field as revealed by PCA and image classification, represented by the classified surface types 1-4 and sulfur at the bottom of Fig. B. C) Thermal infrared temperature map of the fumarole field. D) Simplified thermal structure of the fumarole field highlighting high-temperature fumarole location in red (T > 40 °C) and diffuse thermal activity in green (T = 22-40 °C). The dashed line labeled ALTZ outline demarks the boundary of visible optical effects at the surface and is referred to by us as ALTZ (Alteration Zone). The labels a-g demark notable large-scale anomaly units that can be observed in both, the optical data and thermal data. LTZ 1-3 demark low-temperature zones that separate the high-temperature fumaroles and diffuse active units and cover significant parts of the central fumarole field. Note that the contrast of the background image has been reduced for highlighting in Subfigures B and D.

749
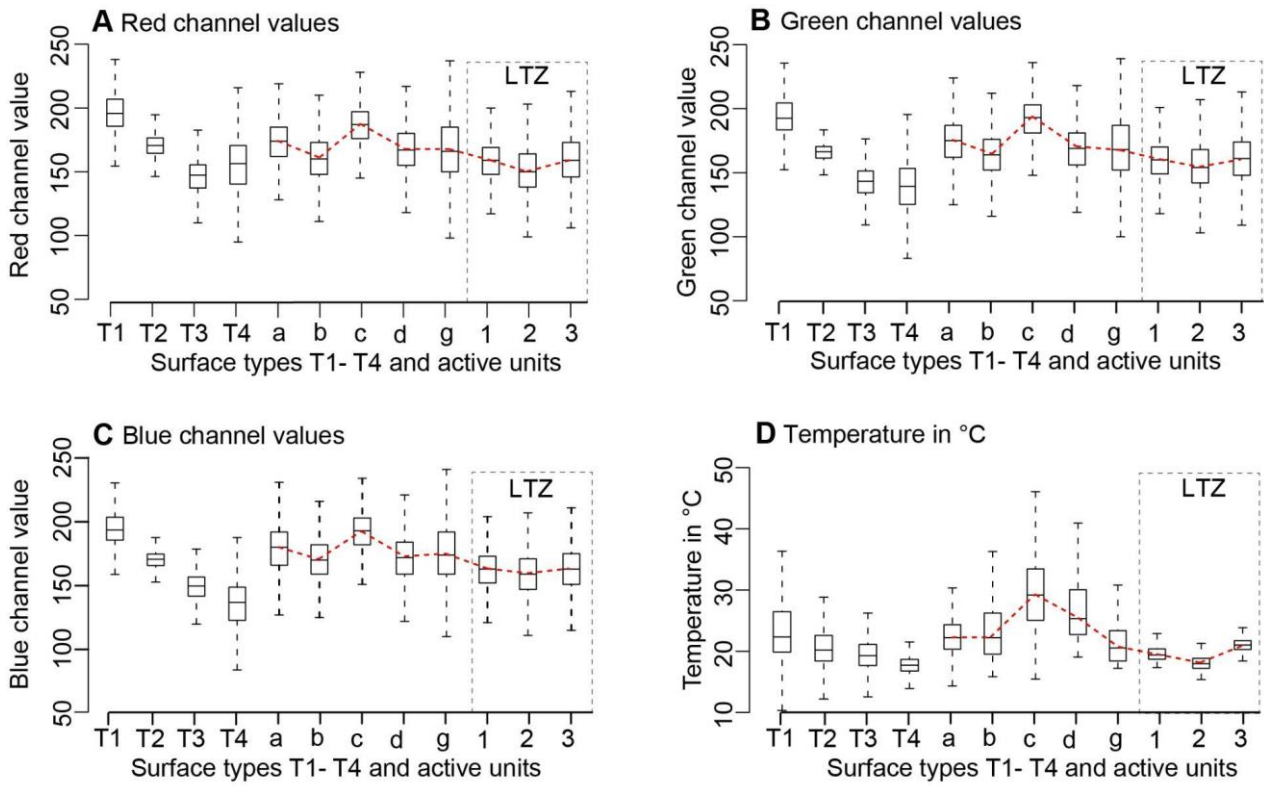
750

751 Figure 5: Boxplots of RGB color value- and temperature distributions observed for the different surface Types 1-4 (T1-T4),

752 identified active units a-g, and associated low-temperature zones LTZ1-3. Surface types and locations of identified units are

753 depicted in Figure 4B/D. A) Red channel value distribution. B) Green channel value distribution. C) Blue channel value

754 distribution. D) Temperature value distribution. Values are based on an analysis of 6.8 million pixels within the ALTZ. Both,

755 the optical (Figure A-C) and thermal (Figure D) value distributions show similarities with generally decreasing values from

756 the T1-T4 surface, a peak in unit c, and low values for LTZ1-3.

757
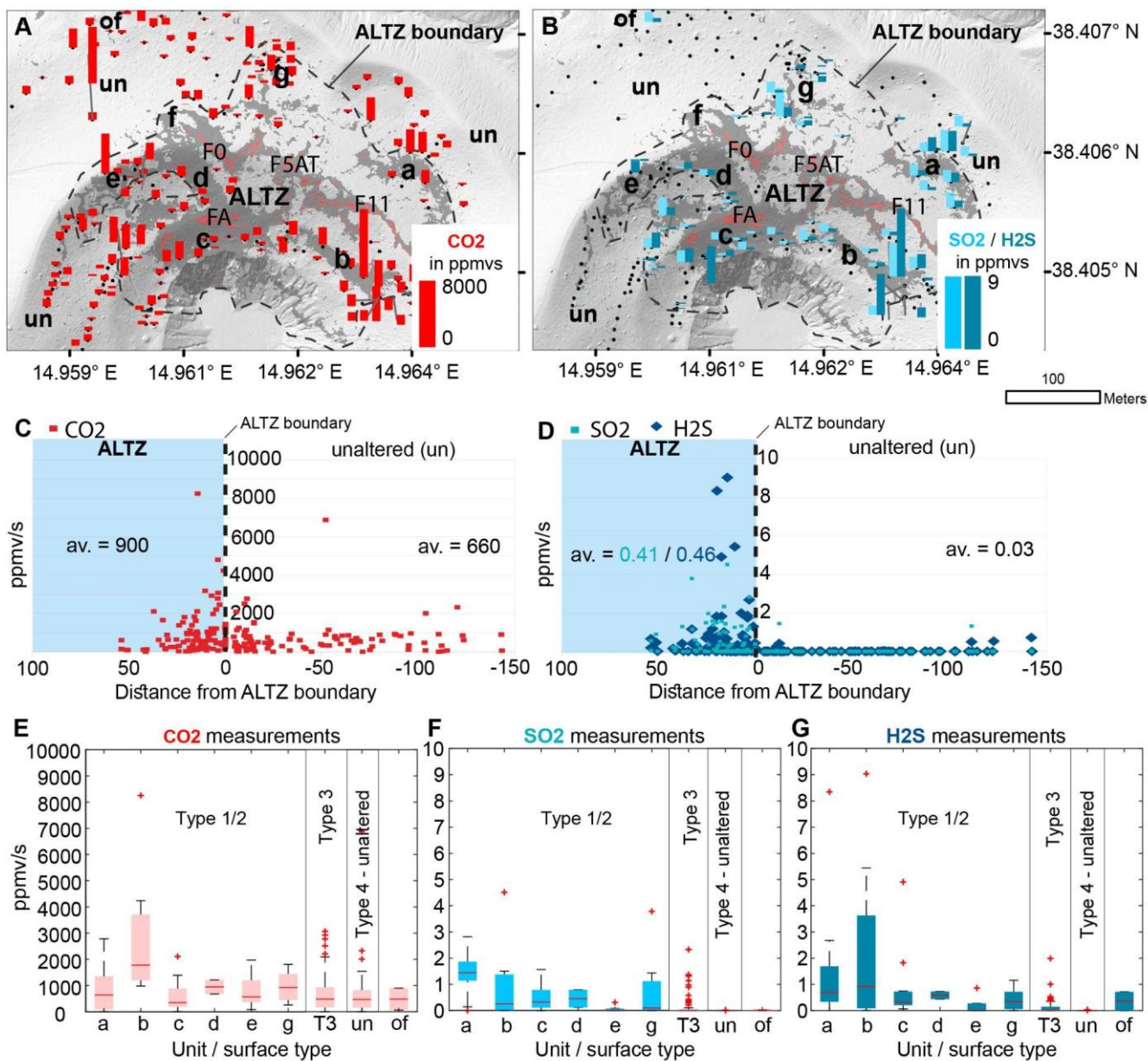
Figure 6: A/B) Spatial distribution and flux values for CO_2 (red bars in A), SO_2 (light blue bars in B), and H_2S (turquoise bars

in B) in a map view for 200 measurement points. Each bar represents a relative flux value at a measurement location. In case

no flux was detectable, the respective location is marked with a black dot only. The dashed line highlights the ALTZ (Alteration

Zone) boundary. Dark grey features in the background highlight the thermally active surface (compare Figure 2D). Labels F0,

F5AT, F11, and FA mark prominent high-temperature fumaroles. The labels a-g mark notable large-scale anomaly units. C/D)

Flux values are plotted by distance to the ALTZ boundary (dashed line). Measurement points within the ALTZ are represented

by positive distances from the ALTZ boundary (highlighted by blue background) and measurements outside the ALTZ by

765   negative distances (unaltered). A generally higher flux is observed within the ALTZ, but while CO_2 is also abundant outside

766   the ALTZ, significant SO_2 and H_2S fluxes were observed exclusively within the ALTZ, especially on the outer edges and

767   associated with units a-g. The averaged flux values (av) are depicted in the respective sections of C and D. E-G) Relative flux

768   values of identified units (a-g), Type 3 surface (T3), the unaltered surface (un), and fumaroles on the northern rim at a distance

769   (of) highlight the spatial variation of different gas species with high flux values for units a and b, lower flux values for e.g.

770   unit c and generally lower flux of sulfuric gas species in the unaltered regime outside the ALTZ.

771
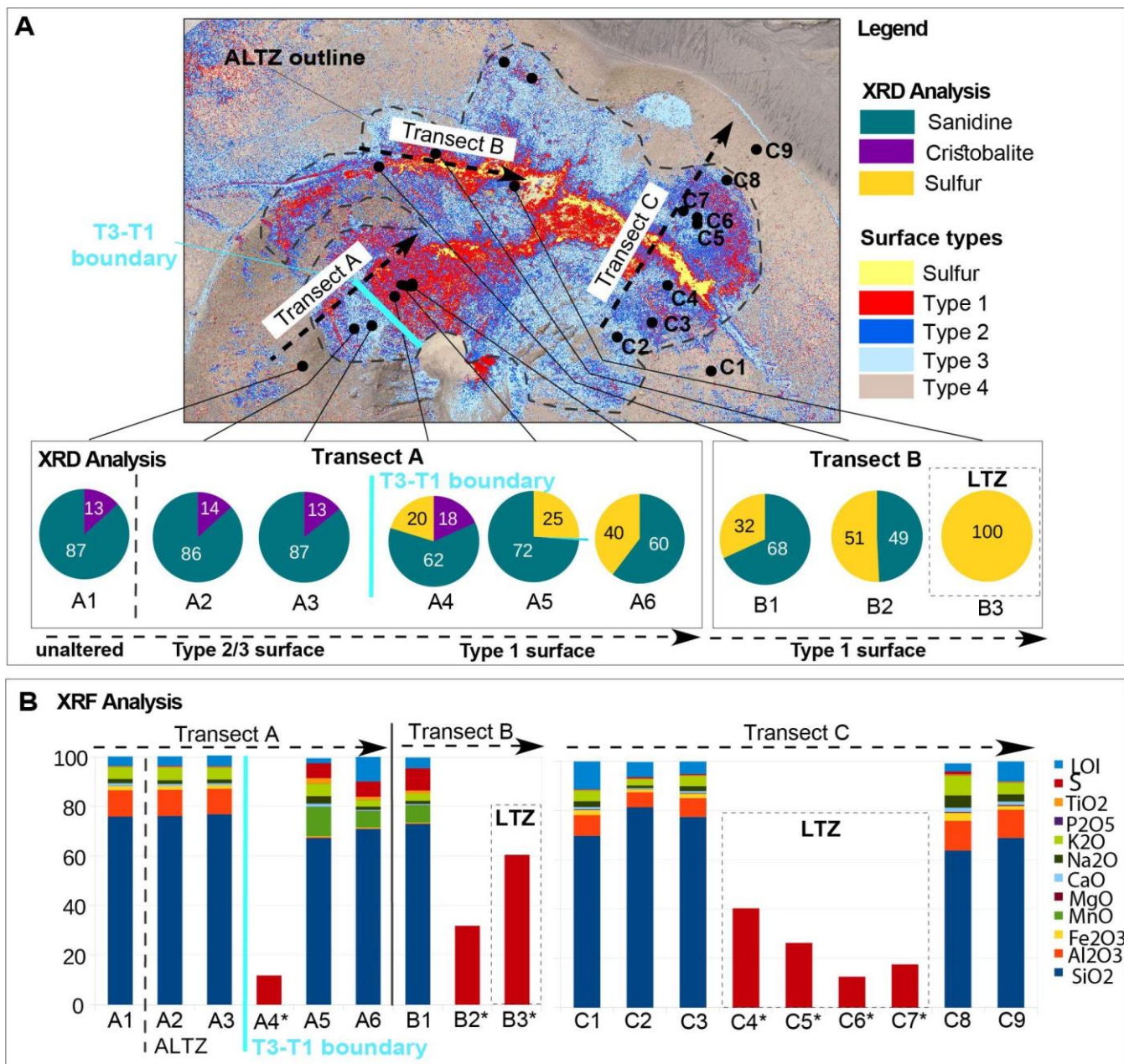
Figure 7: Mineral and bulk chemical composition of rock samples along 3 transects A-C, crosscutting alteration gradients, and structural units. A) Overview map with defined surface types 1-4, highlighting the area with visible optical changes at the surface, referred to as ALTZ (Alteration Zone, marked by a dashed line). The three transects A-C were placed so that they crosscut prominent units. Mineralogical compositions from XRD (X-ray diffraction) are depicted by circular plots at the bottom of Fig. A. B) Bulk chemical composition from XRF (X-ray fluorescence) analysis of transects A-C. Transect A/B) With increasing alteration intensity we observe a relative decrease of the initial mineral phases sanidine and cristobalite whereas the sulfur content increases. Note that the mineral composition in this figure is normalized to 100 % non-amorphous minerals. In the chemical composition, we observe a significant decrease of Al_2O_3 and Fe_2O_3 but an increase of MnO, TiO_2,

781 and S with increasing alteration, especially at the Type3-Type1 (T3-T1) boundary marked in light blue. For transect C we
782 observe a dominant increase of S (17 - 40 %) for samples taken within the LTZ (low-temperature zone). Compared to other
783 transects, changes in Al$_2$O$_3$, Fe$_2$O$_3$, TiO$_2$, and MnO are less significant. For samples marked with an asterisk (*) XRF results
784 are not available. No XRD results are available for transect C.

785
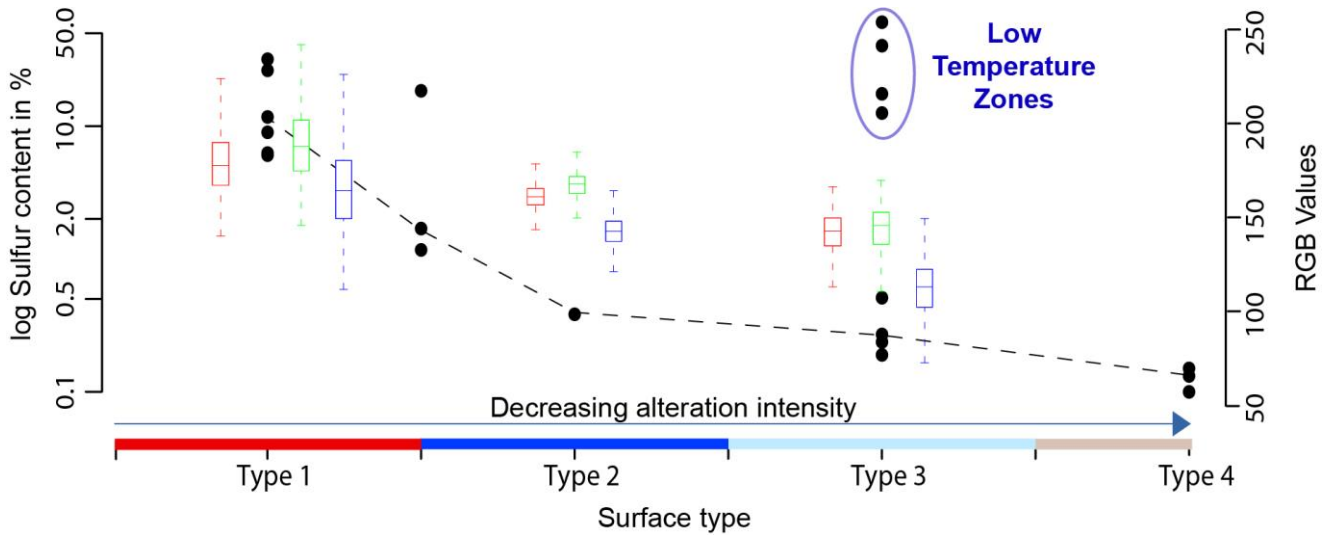
786
787 Figure 8: Relation of inferred surface type (T1-4) and sulfur content of rock samples taken in the respective surface T1-4.
788 Black dots mark the sulfur contents of rock samples and are shown on a log scale versus the surface type from which the
789 sample was taken, labeled by Type 1-4 on the x-axis and demarked with boxes using the same color code as throughout the
790 manuscript. With decreasing alteration from Type 1 surface to Type 4 surface we see a significant decrease of sulfur content
791 from up to 100 % for Type 1 to < 1 % for Type 4 surface. The black dashed line illustrates this. An exemption is the Type 3
792 surface where we observe two distinct clusters, one with low sulfur values and one with exceptionally high sulfur values. These
793 high sulfur values belong to samples taken in the LTZ (low-temperature zones), which separate fumaroles from the larger
794 diffuse active units a and b (compare Figure 4) for instance. These samples indicate that LTZ represent sulfur-rich crusts that
795 block heat and gas flux from the surface. The colored boxplots show the distribution of RGB values for the respective surface
796 Type 1-4, showing a similar trend of decreasing values. Red boxplots represent the red value, blue and green the respective
797 blue and green channel values of the image. The coincidence between both indicates a direct relation or control of sulfur onto
798 the surface colorization.
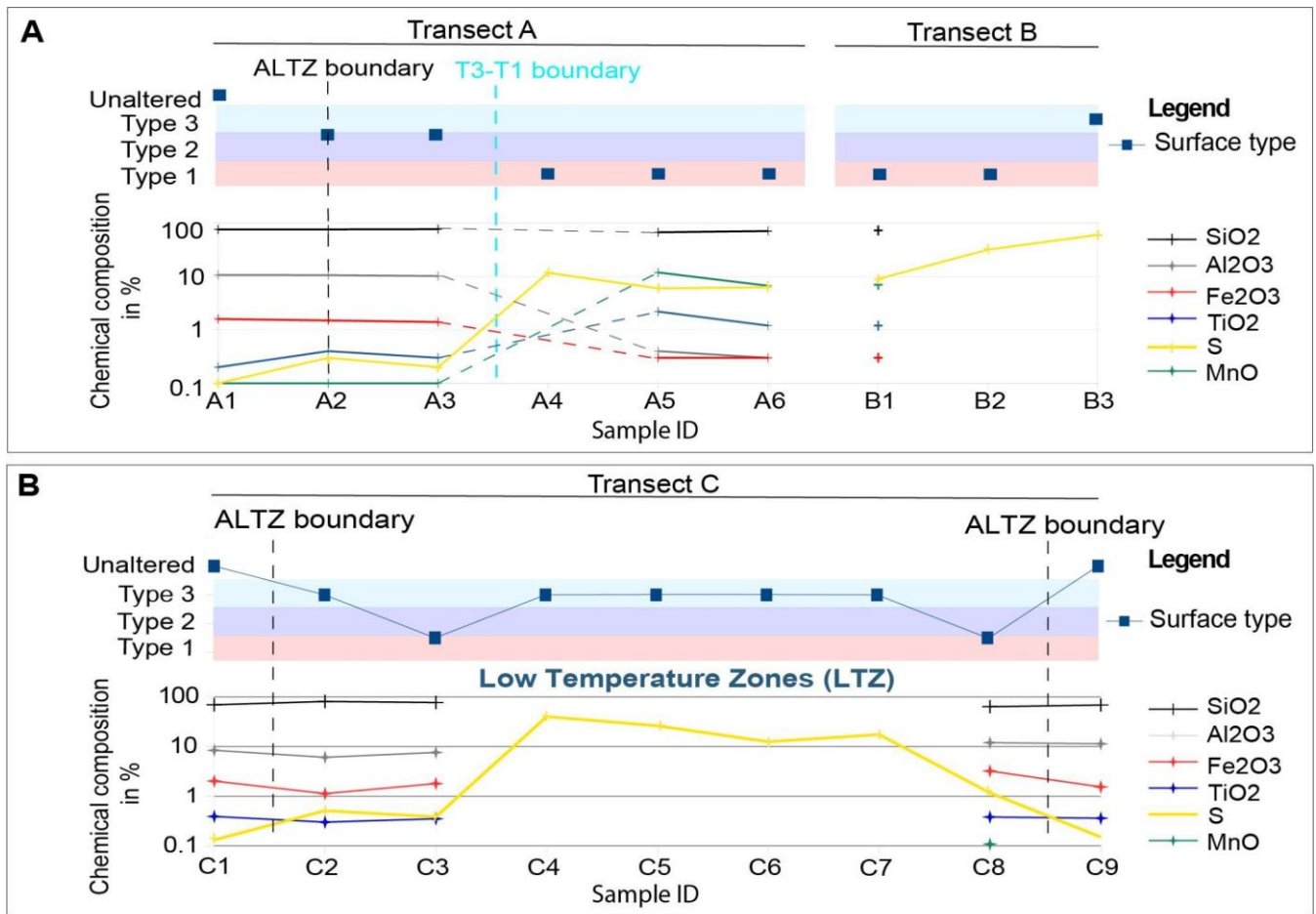
Figure 9: Changes of surface type and bulk-chemical composition observed along transects A, B, and C. Locations for the transects and sample ID are shown in Figure 7. A) With increasing alteration from Type 4 to Type 1 surface we observe a reduction of Fe_2O_3 and Al_2O_3 and an increase in Sulfur. While changes observed at the ALTZ boundary (black dashed line) are only minor, strong changes are observed at the Type 3-Type 1 boundary (T3-T1, blue dashed line). Sulfur contents in transect B were so high that XRF results were only available for sample B1.   B) Changes observed in the eastern fumarole field along transect C are less significant, with the exception of extraordinarily high sulfur content for Type 3 samples collected in the LTZ.
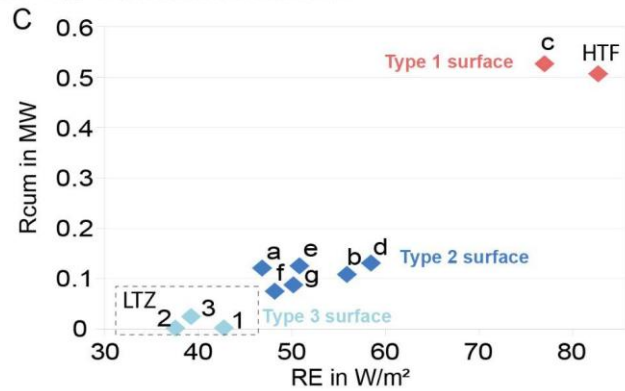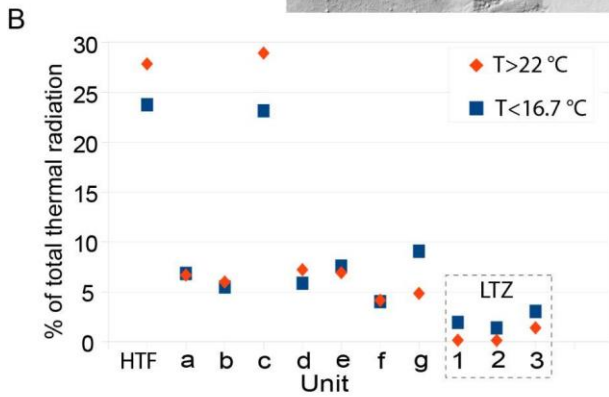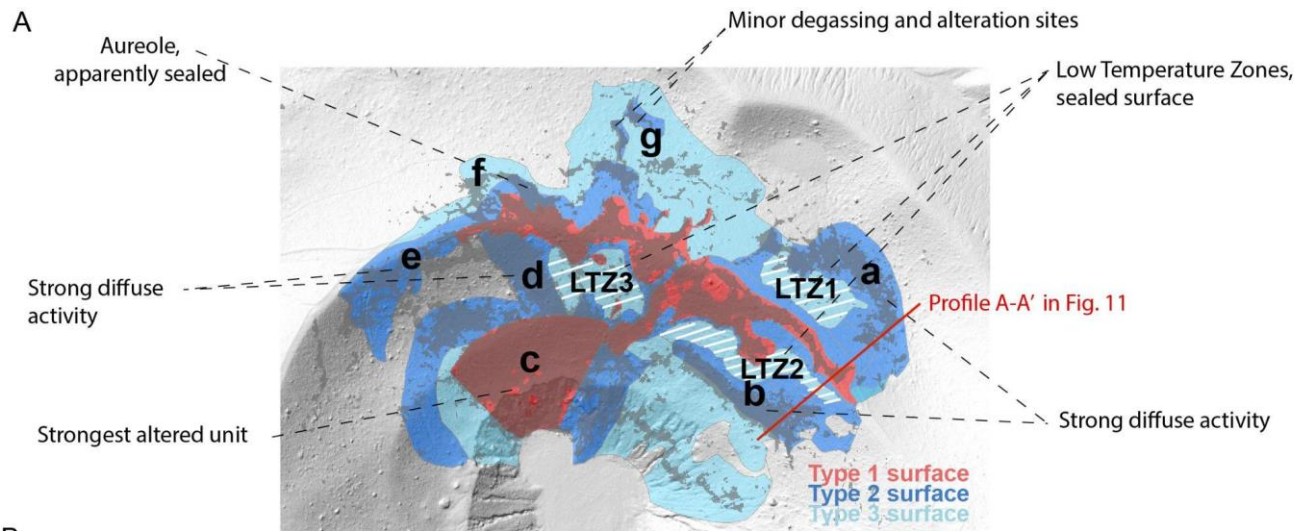
808

809 Figure 10: Anatomy of the fumarole field. A) Simplified structure of the fumarole field highlighting surface types and

810 structural units of increased diffuse activity (a-g) or areas of apparent surface sealing (LTZ1-3 marked by white lines). B)

811 Contribution to the total thermal radiation in % for HTF (high-temperature fumaroles), units a-g, and LTZ1-3 (low-temperature

812 zones) considering pixels with T < 22°C (blue) and for identified units based on a spatial constraint and pixel temperatures >

813 22°C (orange). C) Radiant exitance (RE) in W/m² and cumulative radiation (Rcum) in MW. Rcum is the cumulated

814 background corrected radiant exitance (Equation 2 in the method section) of all pixels associated with the respective active

815 unit. Note that for Rcum only pixels with T > 22°C were used. We can clearly distinguish different thermal regimes that are

816 also coincident with surface types identified in the optical data.

817

818
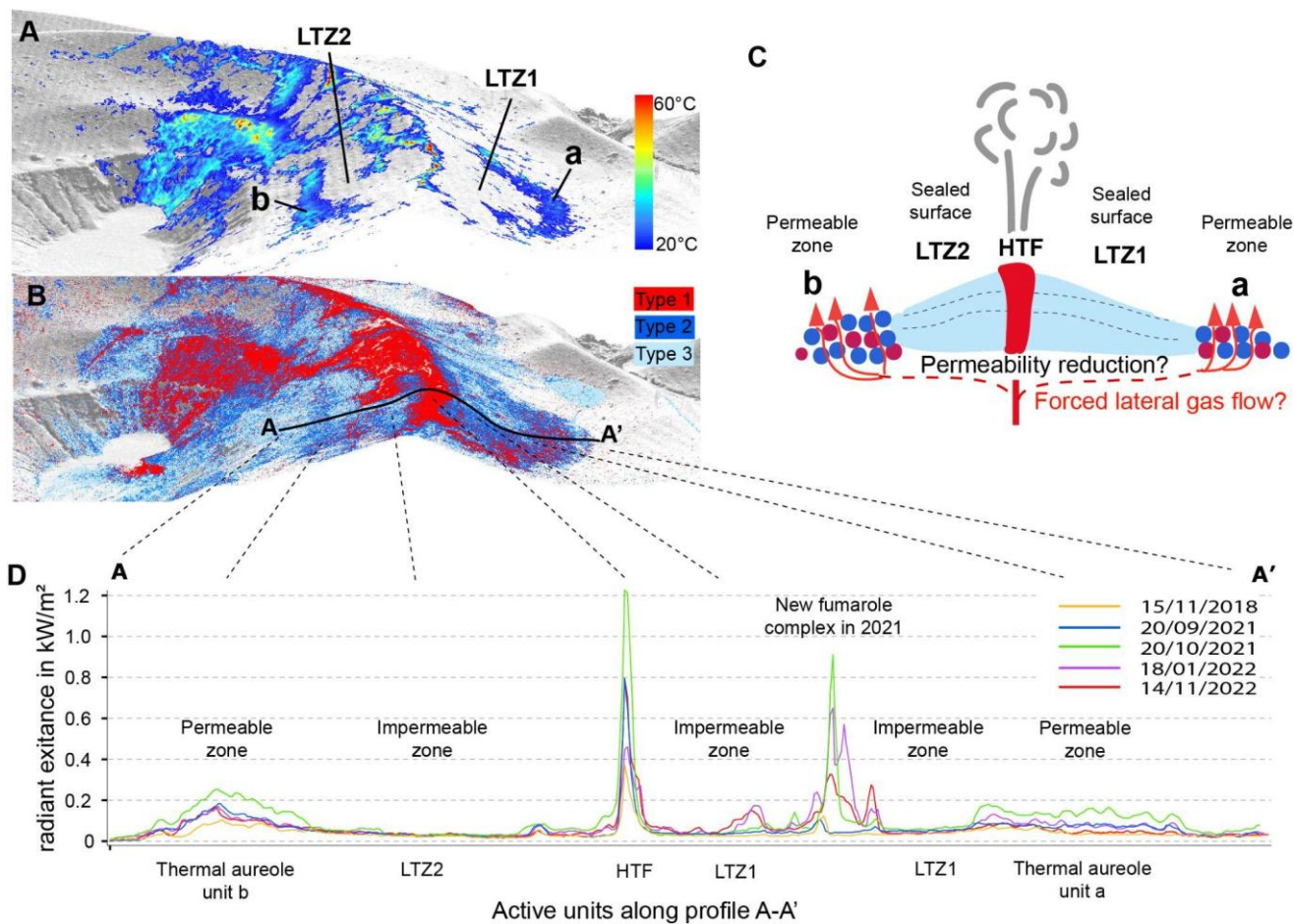
819

820 Figure 11: Cross Section of the eastern fumarole field along Profile A-A' (Fig.10) highlighting the structural setup from high-
821 temperature fumaroles in the center to LTZ and diffuse aureoles at a distance. A) Thermal structure along the cross-section. B)
822 Alteration structure along the cross-section. C) Schematic sketch along cross-section A-A', highlighting the central LTZ that
823 might be controlled by surface sealing processes or deeper effects of permeability reduction in the vicinity to the high-
824 temperature fumaroles due to long-term gas-rock interaction and alteration processes. D) Evolution of thermal radiation values
825 during a volcanic crisis. While thermal radiation at fumaroles and aureoles increased, radiation values of LTZ remained
826 unchanged, therefore highlighting the efficiency of surface sealing.

827

828

829

830

831

832

Appendix A: RGB value distribution of defined surface types 1-3 within the ALTZ
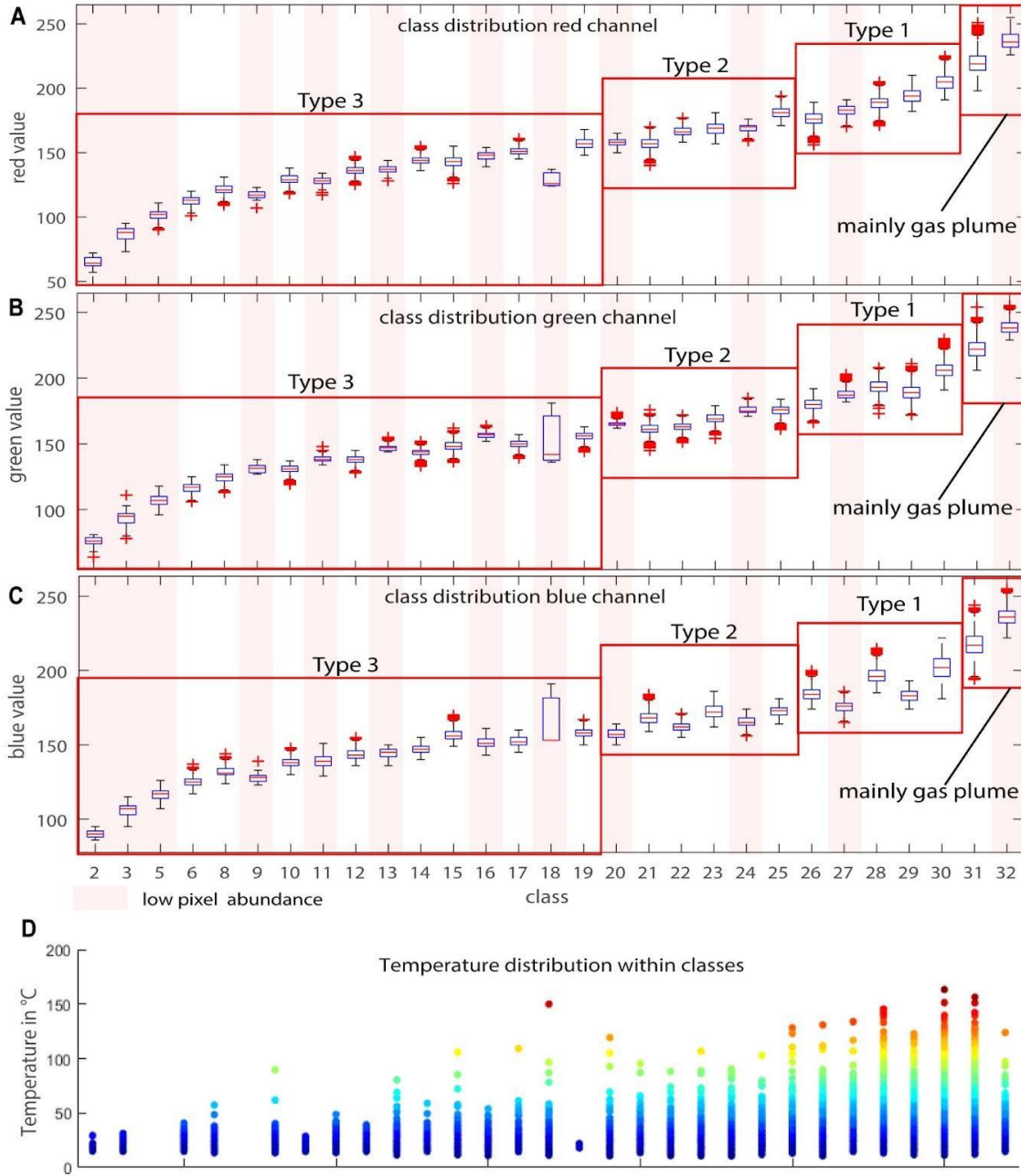
Figure A1: Boxplots of RGB value distribution for the defined surface Types 1-3. Classes (unsupervised classification 32

838 classes) marked with the transparent red bar only have minor pixel abundances. Red boxes depict the spectral range of Type
839 1-3 surfaces. Class 31 and 32 are mainly associated with the fumarole steam plume.

840

841

Appendix B: Gas measurement procedure - simplified accumulation chamber approach
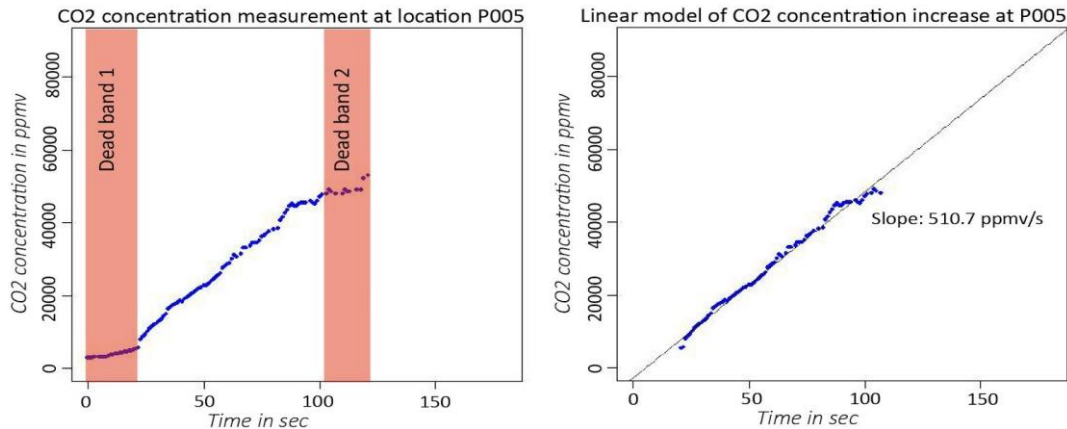
843
844 *Figure B1: CO_2 measurement at location P005, here shown representative for all measurement points. Dead bands at the*
845 *beginning and end of the measurement were removed and the intensity of gas flux was characterized by linear regression*
846 *through the constantly ascending part of the graph. The slopes of the linear model allow a relative comparison of single*
847 *measurement points.*

848

849 To compare the observations from remote sensing to present-day surface degassing, measurement campaigns were performed
850 in September 2021 and November 2022. The surface degassing was measured at 200 points within the northern part of the la
851 fossa cone (Figure 6 in the main manuscript), in a simplified multi-gas accumulation chamber approach.
852 The simplified accumulation chamber consists of the measurement unit, a Dräger Xam 8000, coupled to a 10.3 cm diameter
853 and 16.5 cm long plastic chamber by a 116 cm long tube with an inner diameter of 0.5 cm, resembling a simplified
854 accumulation chamber. The plastic chamber has a volume of 1374.8 cm³, and the tube has a volume of 91.1 cm³ so that the
855 total system volume is 1465.934 cm³. The pumping rate is 0.35l per minute. The plastic chamber was equipped with an open
856 valve which was a necessity as the Dräger is an actively pumping system. Therefore, concentration increases in the chamber
857 can be considered as surface flow and as independent from pumping effects. The Measurement unit is protected by a preceding
858 2µm filter, preventing dust and vapor from entering the unit. Note that we use Flux values in this study only for relative
859 comparison and detection of the spatial variability of certain gas species and flows. A precise flux estimate is beyond the scope
860 of this publication and can not be constrained as we did not measure gas temperatures and humidity at sampling locations.
861 The measurement unit, a Dräger XAM 8000 handheld Multigas device was equipped with 6 sensors measuring CO_2, CH_4,
862 SO_2, H_2S, H_2, and O_2 simultaneously. The relevant species for this work are CO_2, SO_2, and H_2S, therefore only these will be
863 considered in detail. The CO_2 sensor is a Non-Dispersive Infrared (NDIR) sensor. NDIR sensors use the absorption

864 characteristics of CO_2 at ~ 4 μm, which leads to a concentration-dependent amplitude loss of the internally emitted IR light.
865 The sensor has a detection threshold of 0.01 vol% CO_2 and is calibrated for measuring CO_2 in a range of 0-5 vol % at a
866 resolution of 50 ppm under normal (-20-50°C, 10-95 % RH, and 700-1300 hPa) atmospheric conditions. The response rate is
867 < 10 sec for reaching T50- and < 15 sec for reaching T90 concentrations. The H_2S sensor is an electrochemical sensor with a
868 detection limit of 0.4 ppm and a resolution of 0.1 ppm, measuring in a range of 0-100 ppm H_2S under normal atmospheric
869 conditions. The response time for T90 values is >15 seconds and the accuracy of the measurement is +-5 % of the measured
870 value. The SO_2 sensor is an electrochemical sensor with a detection limit of 0.1 ppm and a resolution of 0.1 ppm, measuring
871 as well in a range of 0-100 ppm under atmospheric conditions. The response time for T90 values is < 15 seconds and the
872 accuracy of the measurement is 2 % of the measured value. The NDIR CO_2 sensor is robust against cross-sensitivities.
873 However, electrochemical sensors can be vulnerable to cross sensitivities (SO_2, H_2S, Cl_2), resulting in uncertainties of the
874 measurement of a few percent of the measurement value.
875 The approach of combining the Dräger multigas with an accumulation chamber was developed and adapted as a consequence
876 of uncertainties encountered in previous campaigns. The different sensors have slightly different reaction times for ascending
877 gas concentrations and significantly different reaction times for descending gas concentrations. Comparing sensor readings
878 directly therefore might lead to odd gas ratios. For that reason instead of the direct gas readings, we use the slope of the
879 ascending gas concentration within the accumulation chamber to produce more reliable estimates of the surface flow.
880 For a relative comparison of degassing rates of the single measurement points, the gas data was plotted and the representative
881 part of the graph, resembling a constantly ascending slope, was used to calculate the concentration increase by linear regression.
882 Data points of the "Dead Bands" at the beginning and end of each graph were removed. In this way, we achieve a relative gas
883 flux from soil that allows us to analyze spatial variations of gas flux throughout the study area. An overview of all gas
884 measurement points will be given in Figure 6. The aim of the gas measurements was not to provide accurate flux estimates but
885 to highlight and quantify the spatial variability of the surface flux of certain gas species.
886 Each measurement was performed under similar conditions. Locations were selected in a way that they represent similar
887 surface conditions, considering a spatial distance to fumarolic vents and an unsealed surface, for instance. Measurement
888 locations typically were small areas with a naturally "open surface", often embedded in broader areas of the sealed surface.
889 Such spots typically can be identified by loose gravel on the surface and in case slightly different coloration. For the
890 measurement, the surface was cleaned and gravel was removed to provide a flat contact surface. Then the measurement was
891 started, and the plastic chamber was placed on the ground and sealed on the bottom with fine-grained material. The average
892 measurement duration was 2 min. In case of very rapidly ascending SO_2 or H_2S gas concentrations, the chamber was removed
893 from the ground before and the system was flooded with fresh air, to protect the sensors from critically high acid
894 concentrations. This procedure was chosen to ensure a fresh air flooded chamber at the beginning of each measurement and to
895 record the initial atmospheric gas concentration. Further, it allows better identification of the measurement start- and end-
896 points within the respective data sets, as each data series has two dead bands, one at the beginning and one at the end. Figure
897 B1 shows a typical graph of a CO_2 measurement, with the Dead-Band at the beginning and end of each measurement and the
898 constant ascending graph, representing the gas concentration increase within the chamber. The "Dead Bands" represent parts
899 of the measurement where the accumulation chamber was placed on the ground but not sealed yet, or removed from the soil
900 at the end of the measurements. Dead Bands at the beginning of the measurement were typically on the order of 20- 30 s.

901

Appendix C: Detail views on identified units
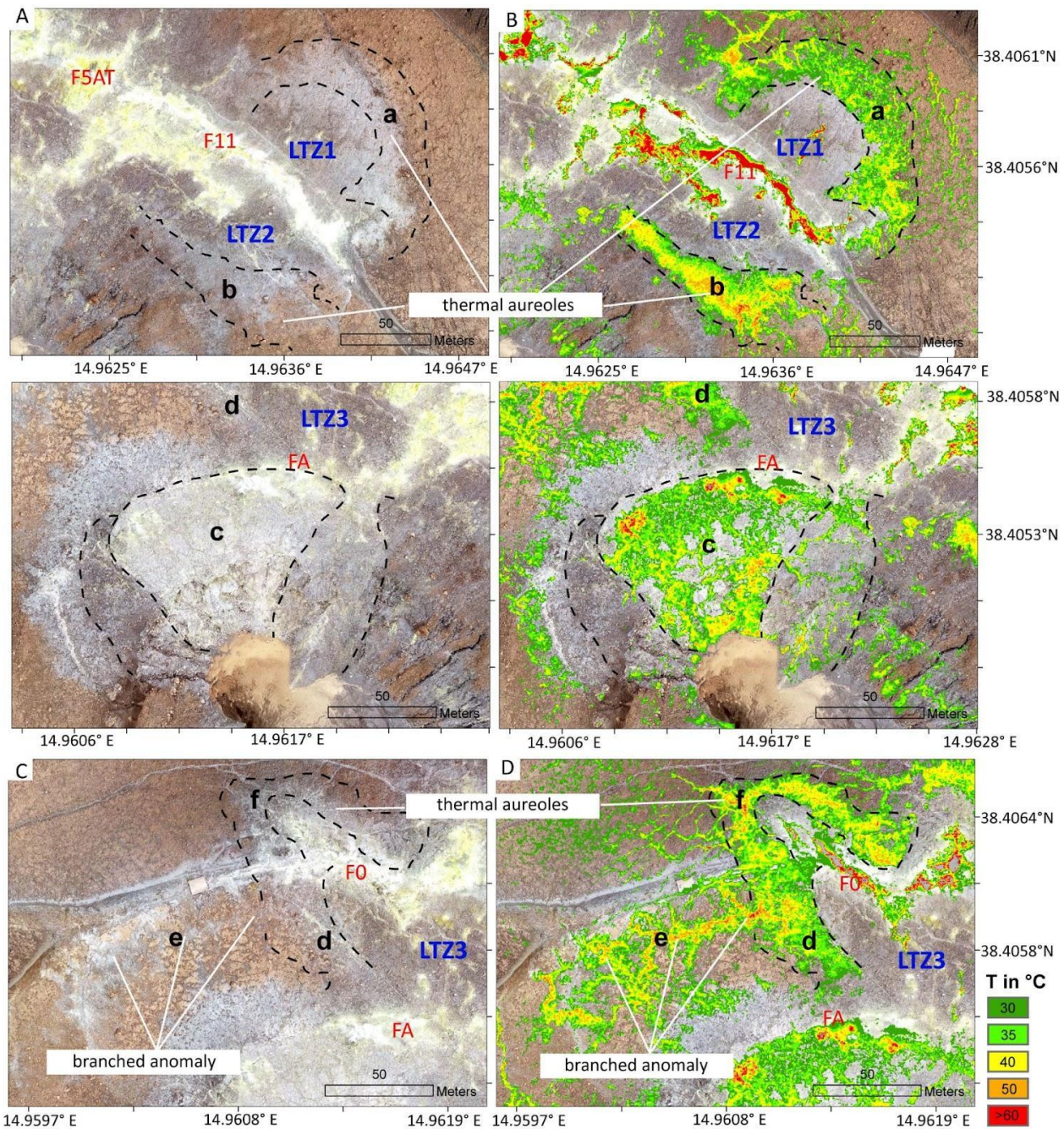
903
Figure C1: Detail views of distinct units a-f and LTZ1-3 in a true color representation as seen from our 2019 orthomosaic data
and an overlay by the thermal data with T > 30 °C. A/B) Shown are units 1 and b and respective LTZ1 and 2. Note the outward
spatial offset of both thermal units with respect to the surface coloration. C/D) Unit c is characterized by a network of thermal

907 anomalies embedded in the colder surroundings. E/F) Thermal aureole d and f branched anomaly e. Also here an outward shift
908 of the thermal feature with respect to the surface coloration is observed, which could indicate gradual sealing processes with
909 proximity to the main vents.

910
911

912 **Appendix D: Spearman correlation test for non-normal distributed variables**

913 The test for correlation between optical and thermal anomalies was performed using the ggpubr package (Kassambara, 2019)
914 in the statistical software environment R. The method used was Spearman's rank correlation which is suggested to be used for
915 non-normal distributed data. The correlation test is based on the vectorized classification raster data set (classp_fumclip) with
916 8,890,830 data points with the analyzed variables pixel class (0-32) and pixel temperature (20- 150°C). The results show a
917 correlation factor of 0.3485299, which is considered a mean positive correlation, and a p-value of 2.2e-16 proves statistical
918 significance.

919

920 Spearman's rank correlation rho
921 data: x and y
922 S = 7.6277e+19, p-value < 2.2e-16
923 alternative hypothesis: true rho is not equal to 0
924 sample estimates:
925 rho
926 0.3485299

927
928

929 **Appendix E: Thermal aureoles and LTZ indicated in field photographs**
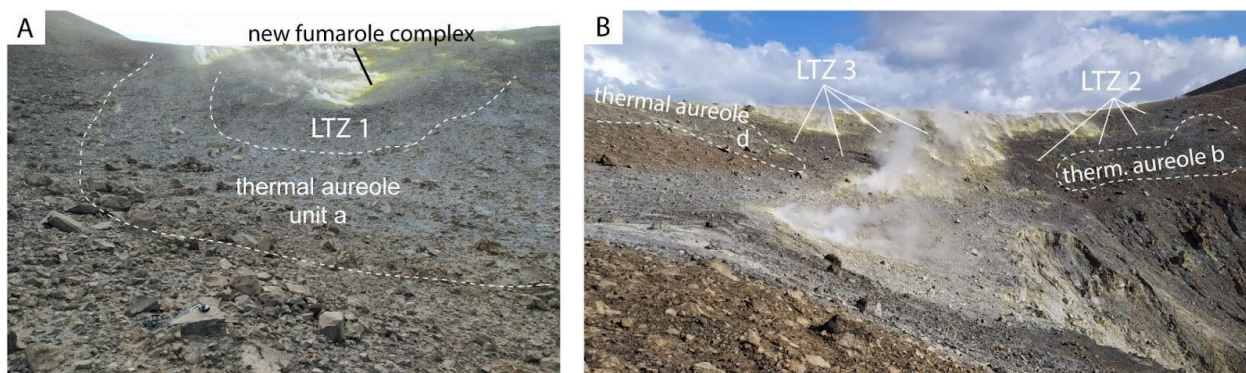
930
931 Figure E1: Thermal aureoles and low-temperature zones (LTZ) depicted on field photographs. A) Thermal aureole a and
932 LTZ1. B) Thermal aureole b and d with LTZ2 and LTZ3.

933
934
935

936 **Appendix F:**

937 Table F1: XRD results of samples taken along transect A and B

Sample ID	A1	A2	A3	A4	A5	A6	B1	B2	B3
Sanidine	86.7	85.7	87.4	61.5	72.2	60.3	68.2	49.2	0
Cristobalite	13.3	14.3	12.6	18.2	0	0	0	0	0
Coesite	0	0	0	0	0.7	0	0	0	0
Sulfur	0	0	0	20.3	25.1	39.7	31.8	50.8	100
amorphous	50	0	0	0	0	50	50	0	0

938
939
940
941 **Appendix G: XRF results of samples taken along transects A-C.**

942 Table G1: XRF results of samples taken along transects A-C. Note that samples with S > 10 % were not analyzed by XRF.

S-ID	SiO_2 (%)	TiO_2 (%)	Al_2O_3 (%)	Fe_2O_3 (%)	MnO (%)	MgO (%)	CaO (%)	Na_2O (%)	K_2O (%)	P_2O_5 (%)	LOI (%)	S Eltra (%)
A1	76.0	0.2	10.7	1.6	0.1	0.1	1.1	1.8	4.8	0.1	3.8	0.1
A2	76.2	0.4	10.6	1.5	0.1	0	0.8	1.5	5.0	0.1	3.9	0.3
A3	77.0	0.3	10.2	1.4	0.1	0	0.7	1.6	4.8	0.1	4.3	0.2
A4	x	x	x	x	x	x	x	x	x	x	x	11.7
A5	67.3	2.2	0.4	0.3	11.9	0.1	1.2	3.1	5.0	0.1	2.0	6.0
A6	71.0	1.2	0.3	0.3	6.7	0.0	0.4	1.3	2.7	0.0	9.8	6.3
B1	73.0	1.2	0.3	0.3	7.0	0.0	0.5	1.3	3.0	0.0	4.3	9.0
B2	x	x	x	x	x	x	x	x	x	x	x	31.9
B3	x	x	x	x	x	x	x	x	x	x	x	60.5
C1	69.7	0.4	8.4	2.0	0	0.3	1.0	2.4	4.2	0.1	11.3	0.1
C2	81.3	0.3	6.1	1.1	0	0.1	0.4	1.1	2.5	0	6.1	0.5

C3	77.4	0.4	7.6	1.8	0	0.2	0.9	2.0	4.0	0.1	5.1	0.4
C4	x	x	x	x	x	x	x	x	x	x	x	40.3
C5	x	x	x	x	x	x	x	x	x	x	x	26.2
C6	x	x	x	x	x	x	x	x	x	x	x	12.5
C7	x	x	x	x	x	x	x	x	x	x	x	17.5
C8	63.8	0.4	12.0	3.2	0.1	0.4	1.7	5.0	8.0	0.1	3.2	1.2
C9	68.9	0.4	11.4	1.5	0	0.4	1.3	3.0	4.7	0.1	8.1	0.2

943
944
10 Data availability

Data will be made available on request for now and will be published on Zenodo in case of acceptance for revision during the revision of this manuscript.

11 Author contributions

D.M conceptualized the study, collected data, performed the remote sensing and gas analysis, and led the manuscript writing. T.R.W. provided funding, supported the conceptualization, and supervised the writing. V.T. supported the conceptualization, performed XRD analysis, and supervised the writing. J.S. performed XRF analysis and supported the writing. A.K. performed XRD analysis and supported the writing. E.D.P. collected data and samples, supported all field works and the writing of this manuscript. A.F.P. supported fieldwork and on the ground logistics, acquired data, and supported the writing. M.Z. supported the gas measurement campaign and supported the writing. B.D.J. supported the fieldwork and writing of this manuscript.

12 Competing interests

The authors declare that they have no conflict of interest.

13 Acknowledgements

We are grateful for the financial and material support provided to realize this study. This work is contributing to the focus site Etna and was financially supported by GFZ Potsdam. Financial support to realize this study was also provided by DAAD research grant Nr. 57556282 and by ERC project 'ROTTnROCK*, a research project funded by the European Research

Council under the European Union's Horizon Europe Programme / ERC synergy grant n. [ERC-2023-SyG 101118491]. We furthermore thank INGV Palermo for collaboration and support, especially during the 2021 crisis, without which parts of this study could not have been realized.

14 References

Abdi, H., & Williams, L. J. (2010). Principal component analysis. Wiley interdisciplinary reviews: computational statistics, 2(4), 433-459. https://doi.org/10.1002/wics.101

Aiuppa, A., Federico, C., Giudice, G., & Gurrieri, S. (2005). Chemical mapping of a fumarolic field: La Fossa crater, Vulcano Island (Aeolian Islands, Italy). Geophysical Research Letters, 32(13). https://doi.org/10.1029/2005GL023207

Alexandris, N., Gupta, S., & Koutsias, N. (2017). Remote sensing of burned areas via PCA, Part 1; centering, scaling and EVD vs SVD. Open geospatial data, software and standards, 2, 1-11. https://doi.org/10.1186/s40965-017-0028-1

Azzarini, F. M., Pareschi, M. T., Sbrana, A., Favalli, M., & Fulignati, P. (2001). Surface hydrothermal alteration mapping at Vulcano Island using MIVIS data. International Journal of Remote Sensing, 22(11), 2045-2070. https://doi.org/10.1080/01431160118291

Ball, M. and Pinkerton, H., 2006. Factors affecting the accuracy of thermal imaging cameras in volcanology. Journal of Geophysical Research: Solid Earth, 111(B11). https://doi.org/10.1029/2005JB003829

Barreca, G., Bruno, V., Cultrera, F., Mattia, M., Monaco, C., & Scarfì, L. (2014). New insights in the geodynamics of the Lipari–Vulcano area (Aeolian Archipelago, southern Italy) from geological, geodetic and seismological data. Journal of Geodynamics, 82, 150-167. https://doi.org/10.1016/j.jog.2014.07.003

Berg, S. E., Troll, V. R., Harris, C., Deegan, F. M., Riishuus, M. S., Burchardt, S., & Krumbholz, M. (2018). Exceptionally high whole-rock δ18O values in intra-caldera rhyolites from Northeast Iceland. Mineralogical Magazine, 82(5), 1147-1168. https://doi.org/10.1180/mgm.2018.114

BILLI, Andrea, et al. Tectonics and seismicity of the Tindari Fault System, southern Italy: Crustal deformations at the transition between ongoing contractional and extensional domains located above the edge of a subducting slab. Tectonics, 2006, 25. Jg., Nr. 2. https://doi.org/10.1029/2004TC001763

Bolognesi, L., & D'Amore, F. (1993). Isotopic variation of the hydrothermal system on Vulcano Island, Italy. Geochimica et Cosmochimica Acta, 57(9), 2069-2082.
https://doi.org/10.1016/0016-7037(93)90094-D

Boyce, A. J., Fulignati, P., Sbrana, A., & Fallick, A. E. (2007). Fluids in early stage hydrothermal alteration of high-sulfidation epithermal systems: A view from the Vulcano active hydrothermal system (Aeolian Island, Italy). Journal of Volcanology and Geothermal Research, 166(2), 76-90.

https://doi.org/10.1016/j.jvolgeores.2007.07.005

Bukumirovic, T., Italiano, F., & Nuccio, P. M. (1997). The evolution of a dynamic geological system: the support of a GIS for geochemical measurements at the fumarole field of Vulcano, Italy. Journal of volcanology and geothermal research, 79(3-4), 253-263. https://doi.org/10.1016/S0377-0273(97)00032-2

Capasso, G., Favara, R., Inguaggiato, S., 1997. Chemical features and isotopic composition of gaseous manifestations on Vulcano Island, Aeolian Islands, Italy: an interpretative model of fluid circulation. Geochim. Cosmochim. Acta 61, 3425–3440 https://doi.org/10.1016/S0016-7037(97)00163-4

Capasso, G., Favara, R., & Inguaggiato, S. (2000). Interaction between fumarolic gases and thermal groundwaters at Vulcano Island (Italy): evidences from chemical composition of dissolved gases in waters. Journal of volcanology and geothermal research, 102(3-4), 309-318. https://doi.org/10.1016/S0377-0273(00)00193-1

Capasso, G., Federico, C., Madonia, P., & Paonita, A. (2014). Response of the shallow aquifer of the volcano-hydrothermal system during the recent crises at Vulcano Island (Aeolian Archipelago, Italy). Journal of volcanology and geothermal research, 273, 70-80. https://doi.org/10.1016/j.jvolgeores.2014.01.005

Carapezza, M. L., Barberi, F., Ranaldi, M., Ricci, T., Tarchini, L., Barrancos, J., ... & Gattuso, A. (2011). Diffuse CO2 soil degassing and CO2 and H2S concentrations in air and related hazards at Vulcano Island (Aeolian arc, Italy). Journal of Volcanology and Geothermal Research, 207(3-4), 130-144. https://doi.org/10.1016/j.jvolgeores.2011.06.010

Carranza, E. J. M., & Hale, M. (2002). Mineral imaging with Landsat Thematic Mapper data for hydrothermal alteration mapping in heavily vegetated terrane. International journal of remote sensing, 23(22), 4827-4852. https://doi.org/10.1080/01431160110115014

Chiodini, G., Cioni, R., & Marini, L. (1993). Reactions governing the chemistry of crater fumaroles from Vulcano Island, Italy, and implications for volcanic surveillance. Applied Geochemistry, 8(4), 357-371. https://doi.org/10.1016/0883-2927(93)90004-Z

Chiodini G., Cioni R., Marini L. and Panichi C. (1995) Origin of fumarolic fluids of Vulcano Island, Italy and implications for volcanic surveillance. Bull. Volcanol. 57, 99–110. http://dx.doi.org/10.1007/BF00301400

Chiodini, G., Allard, P., Caliro, S., Parello, F., 2000. 18O exchange between steam and carbon dioxide in volcanic and hydrothermal gases: Implications for the source of water. Geochim. Cosmochim. Acta 64, 2479–2488 https://doi.org/10.1016/S0016-7037(99)00445-7

Chiodini, G., Frondini, F., & Raco, B. (1996). Diffuse emission of CO 2 from the Fossa crater, Vulcano Island (Italy). Bulletin of Volcanology, 58, 41-50. https://doi.org/10.1007/s004450050124

Chiodini, G., Granieri, D., Avino, R., Caliro, S., Costa, A., & Werner, C. (2005). Carbon dioxide diffuse degassing and estimation of heat release from volcanic and hydrothermal systems. Journal of Geophysical Research: Solid Earth, 110(B8). https://doi.org/10.1029/2004JB003542

Clarke, A. B., Ongaro, T. E., & Belousov, A. (2015). Vulcanian eruptions. In The encyclopedia of volcanoes (pp. 505-518). Academic Press. https://doi.org/10.1016/B978-0-12-385938-9.00028-6

Coppola, D., Laiolo, M., Campus, A., & Massimetti, F. (2022). Thermal unrest of a fumarolic field tracked using VIIRS imaging bands: The case of La fossa crater (Vulcano Island, Italy). Frontiers in Earth Science, 10, 964372. https://doi.org/10.3389/feart.2022.964372

Cultrera F., Barreca G., Ferranti L., Monaco C., Pepe F., Passaro S., Barberi G., Bruno V., Burrato P., Mattia M., Musumeci C., Scarfì L.; Structural architecture and active deformation pattern in the northern sector of the Aeolian-Tindari-Letojanni fault system (SE Tyrrhenian Sea-NE Sicily) from integrated analysis of field, marine geophysical, seismological and geodetic data. Italian Journal of Geosciences 2017;; 136 (3): 399–417. https://doi.org/10.3301/IJG.2016.17

Darmawan, H., Troll, V. R., Walter, T. R., Deegan, F. M., Geiger, H., Heap, M. J., ... & Müller, D. (2022). Hidden mechanical weaknesses within lava domes provided by buried high-porosity hydrothermal alteration zones. Scientific Reports, 12(1), 3202. https://doi.org/10.1038/s41598-022-06765-9

De Astis, G., La Volpe, L., Peccerillo, A., & Civetta, L. (1997). Volcanological and petrological evolution of Vulcano island (Aeolian Arc, southern Tyrrhenian Sea). Journal of Geophysical Research: Solid Earth, 102(B4), 8021-8050. https://doi.org/10.1029/96JB03735

De Astis, G., Lucchi, F., Dellino, P., La Volpe, L., Tranne, C. A., Frezzotti, M. L., & Peccerillo, A. (2013). Chapter 11 Geology, volcanic history and petrology of Vulcano (central Aeolian archipelago). Geological Society, London, Memoirs, 37(1), 281-349. https://doi.org/10.1144/M37.11

Di Tommaso, I., & Rubinstein, N. (2007). Hydrothermal alteration mapping using ASTER data in the Infiernillo porphyry deposit, Argentina. Ore Geology Reviews, 32(1-2), 275-290. https://doi.org/10.1016/j.oregeorev.2006.05.004

Diliberto, I. S. (2013). Time series analysis of high temperature fumaroles monitored on the island of Vulcano (Aeolian Archipelago, Italy). Journal of volcanology and geothermal research, 264, 150-163. https://doi.org/10.1016/j.jvolgeores.2013.08.003

Diliberto, I. S. (2017). Long-term monitoring on a closed-conduit volcano: A 25 year long time-series of temperatures recorded at La Fossa cone (Vulcano Island, Italy), ranging from 250 C to 520 C. Journal of Volcanology and Geothermal Research, 346, 151-160. https://doi.org/10.1016/j.jvolgeores.2017.03.005

Diliberto, I., Pedone, M., Jácome Paz, M., Inguaggiato, S., Mazot, A., Cangemi, M. and Pisciotta, A.F., 2021. Volcanic Gas Hazard Assessment in the Baia di Levante Area (Vulcano Island, Italy) Inferred by Geochemical Investigation of Passive Fluid Degassing. Environmental Geosciences, 11.

1084   https://doi.org/10.3390/geosciences11110478

1085

1086   Donoghue, E., Troll, V. R., Harris, C., O'Halloran, A., Walter, T. R., & Torrado, F. J. P. (2008). Low-temperature hydrothermal
1087   alteration of intra-caldera tuffs, Miocene Tejeda caldera, Gran Canaria, Canary Islands. Journal of Volcanology and
1088   Geothermal Research, 176(4), 551-564. https://doi.org/10.1016/j.jvolgeores.2008.05.002

1089

1090   Donoghue, E., Troll, V. R., & Harris, C. (2010). Fluid–rock interaction in the Miocene, Post-Caldera, Tejeda intrusive
1091   complex, Gran Canaria (Canary Islands): insights from mineralogy, and O-and H-isotope geochemistry. Journal of Petrology,
1092   51(10), 2149-2176. https://doi.org/10.1093/petrology/egq052

1093

1094   Fauvel, M., Chanussot, J., & Benediktsson, J. A. (2009). Kernel principal component analysis for the classification of
1095   hyperspectral remote sensing data over urban areas. EURASIP Journal on Advances in Signal Processing, 2009, 1-14.

1096

1097   Fischer, T. P., Ramírez, C., Mora-Amador, R. A., Hilton, D. R., Barnes, J. D., Sharp, Z. D., ... & Shaw, A. M. (2015). Temporal
1098   variations in fumarole gas chemistry at Poás volcano, Costa Rica. Journal of Volcanology and Geothermal Research, 294, 56-
1099   70. https://doi.org/10.1016/j.jvolgeores.2015.02.002

1100

1101   *Frolova, et al. Effects of hydrothermal alterations on physical and mechanical properties of rocks in the Kuril–Kamchatka*
1102   *island arc. Engineering Geology, 2014, 183. Jg., S. 80-95.*
1103   https://doi.org/10.1016/j.enggeo.2014.10.011

1104

1105   Fulignati, P., Gioncada, A., & Sbrana, A. (1998). Geologic model of the magmatic-hydrothermal system of vulcano (Aeolian
1106   Islands, Italy). Mineralogy and Petrology, 62(3-4), 195.

1107

1108   Fulignati, P., Gioncada, A., & Sbrana, A. (1999). Rare-earth element (REE) behaviour in the alteration facies of the active
1109   magmatic–hydrothermal system of Vulcano (Aeolian Islands, Italy). Journal of Volcanology and geothermal research, 88(4),
1110   325-342. https://doi.org/10.1016/S0377-0273(98)00117-6

1111

1112   Fulignati, P. (2020). Clay minerals in hydrothermal systems. Minerals, 10(10), 919. https://doi.org/10.3390/min10100919

1113

1114   Gertisser, R., Troll, V. R., Walter, T. R., Nandaka, I. G. M. A., & Ratdomopurbo, A. (Eds.). (2023). Merapi Volcano: Geology,
1115   Eruptive Activity, and Monitoring of a High-Risk Volcano. Springer Nature.
1116   https://doi.org/10.1007/978-3-031-15040-1

1117

1118   Giggenbach, W.F. (1996). Chemical Composition of Volcanic Gases. In: Monitoring and Mitigation of Volcano Hazards.
1119   Springer, Berlin, Heidelberg. https://doi.org/10.1007/978-3-642-80087-0_7

1120

1121   Halldórsson, S. A., Hilton, D. R., Troll, V. R., & Fischer, T. P. (2013). Resolving volatile sources along the western Sunda
1122   arc, Indonesia. Chemical Geology, 339, 263-282. https://doi.org/10.1016/j.chemgeo.2012.09.042

1123

1124   Harris, A. J., Lodato, L., Dehn, J., & Spampinato, L. (2009). Thermal characterization of the Vulcano fumarole field. Bulletin
1125   of Volcanology, 71, 441-458. https://doi.org/10.1007/s00445-008-0236-8

Harris, A., Alparone, S., Bonforte, A., Dehn, J., Gambino, S., Lodato, L., & Spampinato, L. (2012). Vent temperature trends at the Vulcano Fossa fumarole field: the role of permeability. Bulletin of volcanology, 74, 1293-1311. https://doi.org/10.1007/s00445-012-0593-1

Heap, M.J., Troll, V.R., Kushnir, A.R.L., Gilg, H.A., Collinson, A.S.D., Deegan, F.M., Darmawan, H., Seraphine, N., Neuberg, J. and Walter, T.R., 2019. Hydrothermal alteration of andesitic lava domes can lead to explosive volcanic behaviour. Nature Communications, 10(1): 5063. https://doi.org/10.1038/s41467-019-13102-8

Heap, M. J., & Violay, M. E. (2021). The mechanical behaviour and failure modes of volcanic rocks: a review. Bulletin of Volcanology, 83(5), 33. https://doi.org/10.1007/s00445-021-01447-2

Heap, M. J., Baumann, T. S., Rosas-Carbajal, M., Komorowski, J. C., Gilg, H. A., Villeneuve, M., ... & Reuschlé, T. (2021). Alteration-Induced Volcano Instability at La Soufrière de Guadeloupe (Eastern Caribbean). Journal of Geophysical Research: Solid Earth, 126(8), e2021JB022514. https://doi.org/10.1029/2021JB022514

Heap, M. J., Baumann, T., Gilg, H. A., Kolzenburg, S., Ryan, A. G., Villeneuve, M., ... & Clynne, M. A. (2021). Hydrothermal alteration can result in pore pressurization and volcano instability. Geology, 49(11), 1348-1352. https://doi.org/10.1130/G49063.1

Henley, R. W., & McNabb, A. (1978). Magmatic vapor plumes and ground-water interaction in porphyry copper emplacement. Economic Geology, 73(1), 1-20. https://doi.org/10.2113/gsecongeo.73.1.1

Inguaggiato, S., Vita, F., Diliberto, I. S., Inguaggiato, C., Mazot, A., Cangemi, M., & Corrao, M. (2022). The volcanic activity changes occurred in the 2021–2022 at Vulcano island (Italy), inferred by the abrupt variations of soil CO_2 output. Scientific Reports, 12(1), 21166. https://doi.org/10.3390/rs14051283

Kassambara, A. (2020). ggpubr:'ggplot2'based publication ready plots. R package version 0.4. 0.

Kereszturi, G., Schaefer, L. N., Miller, C., & Mead, S. (2020). Hydrothermal alteration on composite volcanoes: mineralogy, hyperspectral imaging, and aeromagnetic study of Mt Ruapehu, New Zealand. Geochemistry, Geophysics, Geosystems, 21(9), e2020GC009270. https://doi.org/10.1029/2020GC009270

Liuzzo, M., Di Muro, A., Giudice, G., Michon, L., Ferrazzini, V., & Gurrieri, S. (2015). New evidence of CO_2 soil degassing anomalies on P iton de la F ournaise volcano and the link with volcano tectonic structures. Geochemistry, Geophysics, Geosystems, 16(12), 4388-4404. https://doi.org/10.1002/2015GC006032

Loughlin, W. P. (1991). Principal component analysis for alteration mapping. Photogrammetric Engineering and Remote Sensing, 57(9), 1163-1169.

Lynch, D.K., Hudnut, K.W. and Adams, P.M., 2013. Development and growth of recently-exposed fumarole fields near Mullet Island, Imperial County, California. Geomorphology, 195: 27-44. https://doi.org/10.1016/j.geomorph.2013.04.022

Madonia, P., Cusano, P., Diliberto, I. S., & Cangemi, M. (2013). Thermal anomalies in fumaroles at Vulcano island (Italy) and their relationship with seismic activity. Physics and Chemistry of the Earth, Parts A/B/C, 63, 160-169. https://doi.org/10.1016/j.pce.2013.06.001

Madonia, P., Cangemi, M., Costa, M., & Madonia, I. (2016). Mapping fumarolic fields in volcanic areas: A methodological approach based on the case study of La Fossa cone, Vulcano island (Italy). Journal of volcanology and geothermal research, 324, 1-7. https://doi.org/10.1016/j.jvolgeores.2016.05.014

Mannini, S., Harris, A. J., Jessop, D. E., Chevrel, M. O., & Ramsey, M. S. (2019). Combining ground-and ASTER-based thermal Measurements to Constrain fumarole field heat budgets: The case of Vulcano Fossa 2000–2019. Geophysical Research Letters, 46(21), 11868-11877. https://doi.org/10.1029/2019GL084013

Mia, B., & Fujimitsu, Y. (2012). Mapping hydrothermal altered mineral deposits using Landsat 7 ETM+ image in and around Kuju volcano, Kyushu, Japan. Journal of Earth System Science, 121, 1049-1057. https://doi.org/10.1007/s12040-012-0211-9

Middlemost, E. A. (1994). Naming materials in the magma/igneous rock system. Earth-science reviews, 37(3-4), 215-224. https://doi.org/10.1016/0012-8252(94)90029-9

Minissale, A., Donato, A., Procesi, M., Pizzino, L. and Giammanco, S., 2019. Systematic review of geochemical data from thermal springs, gas vents and fumaroles of Southern Italy for geothermal favourability mapping. Earth-Sci Rev, 188: 514-535. https://doi.org/10.1016/j.earscirev.2018.09.008

Müller, D., Bredemeyer, S., Zorn, E., De Paolo, E., & Walter, T. R. (2021). Surveying fumarole sites and hydrothermal alteration by unoccupied aircraft systems (UAS) at the La Fossa cone, Vulcano Island (Italy). Journal of Volcanology and Geothermal Research, 413, 107208. https://doi.org/10.1016/j.jvolgeores.2021.107208

Nuccio, P. M., & Paonita, A. (2001). Magmatic degassing of multicomponent vapors and assessment of magma depth: application to Vulcano Island (Italy). Earth and Planetary Science Letters, 193(3-4), 467-481. https://doi.org/10.1016/S0012-821X(01)00512-X

Paonita, A., Federico, C., Bonfanti, P., Capasso, G., Inguaggiato, S., Italiano, F., ... & Sortino, F. (2013). The episodic and abrupt geochemical changes at La Fossa fumaroles (Vulcano Island, Italy) and related constraints on the dynamics, structure, and compositions of the magmatic system. Geochimica et Cosmochimica Acta, 120, 158-178. https://doi.org/10.1016/j.gca.2013.06.015

Pearson, K. F.R.S. (1901). LIII. On lines and planes of closest fit to systems of points in space. The London, Edinburgh, and Dublin Philosophical Magazine and Journal of Science, 2(11), 559–572. https://doi.org/10.1080/14786440109462720

Pirajno, F. (2009). Hydrothermal Processes and Wall Rock Alteration. In: Hydrothermal Processes and Mineral Systems. Springer, Dordrecht. https://doi.org/10.1007/978-1-4020-8613-7_2

Reid, M. E., Sisson, T. W., & Brien, D. L. (2001). Volcano collapse promoted by hydrothermal alteration and edifice shape, Mount Rainier, Washington. Geology, 29(9), 779-782. https://doi.org/10.1130/0091-7613(2001)029%3C0779:VCPBHA%3E2.0.CO;2

Rowan, L. C., Wetlaufer, P. H., & Stewart, J. H. (1976). Discrimination of rock Types and detection of hydrothermally altered areas in south-central Nevada by the use of computer-enhanced ERTS images.

Silvestri, M., Rabuffi, F., Pisciotta, A., Musacchio, M., Diliberto, I. S., Spinetti, C., ... & Buongiorno, M. F. (2019). Analysis of thermal anomalies in volcanic areas using multiscale and multitemporal monitoring: Vulcano island test case. Remote Sensing, 11(2), 134. https://doi.org/10.3390/rs11020134

Stevenson, J.A. and Varley, N., 2008. Fumarole monitoring with a handheld infrared camera: Volcán de Colima, Mexico, 2006–2007. Journal of Volcanology and Geothermal Research, 177(4), pp.911-924. https://doi.org/10.1016/j.jvolgeores.2008.07.003

Tayebi, M.H., Tangestani, M.H. & Vincent, R.K. Sub-pixel mapping of iron-bearing minerals using ALI data and MTMF algorithm, Masahim volcano, SE Iran. Arab J Geosci 8, 3799–3810 (2015). https://doi.org/10.1007/s12517-014-1400-4

Troll, V. R., Hilton, D. R., Jolis, E. M., Chadwick, J. P., Blythe, L. S., Deegan, F. M., ... & Zimmer, M. (2012). Crustal CO_2 liberation during the 2006 eruption and earthquake events at Merapi volcano, Indonesia. Geophysical Research Letters, 39(11). https://doi.org/10.1029/2012GL051307

Toutain, J.-P., Sortino, F., Baubron, J.-C., Richon, P., Surono, Sumarti, S. and Nonell, A., 2009. Structure and CO_2 budget of Merapi volcano during inter-eruptive periods. B Volcanol, 71(7): 815-826. https://doi.org/10.1007/s00445-009-0266-x

Van der Meer, F. D., Van der Werff, H. M., Van Ruitenbeek, F. J., Hecker, C. A., Bakker, W. H., Noomen, M. F., ... & Woldai, T. (2012). Multi-and hyperspectral geologic remote sensing: A review. International Journal of Applied Earth Observation and Geoinformation, 14(1), 112-128. https://doi.org/10.1016/j.jag.2011.08.002